

A novel framework to model the fatigue behavior of brittle materials based on a variational phase-field approach

P. Carrara^{a,*}, M. Ambati^a, R. Alessi^b, L. De Lorenzis^a

^a*Technische Universität Braunschweig, Institute of Applied Mechanics, Pockelsstr. 3, 38106 Braunschweig, Germany*

^b*Università di Pisa, Department of Civil and Industrial Engineering, Largo Lucio Lazzarino, 56122 Pisa, Italy*

Abstract

A novel variational framework to model the fatigue behavior of brittle materials based on a phase-field approach to fracture is presented. The standard regularized free energy functional is modified introducing a fatigue degradation function that effectively reduces the fracture toughness as a proper history variable accumulates. This macroscopic approach allows to reproduce the main known features of fatigue crack growth in brittle materials. Numerical experiments show that the Wöhler curve, the crack growth rate curve and the Paris law are naturally recovered, while the approximate Palmgren-Miner criterion and the monotonic loading condition are obtained as special cases.

Keywords: Brittle fracture, Fatigue, Paris law, Phase-field models, Wöhler curve

1. Introduction and state of the art

The term fatigue refers to repeatedly applied macroscopic loads or displacements whose maximum value is below the monotonic strength of the material [1]. When a component is subjected to fatigue loading (cyclic or not), it experiences, at first, the formation of microdefects (e.g., microvoids) at micro-heterogeneities such as pits or imperfections. Depending on the type of material, within this phase energetic barriers that inhibit the microdefects evolution when the load level is below a so-called fatigue threshold might be

*Corresponding author

Email address: p.carrara@tu-braunschweig.de (P. Carrara)

present [2, 3]. When the fatigue process advances, the microdefects evolve into microcracks. These early processes are ruled by the stochastic microstructural arrangement of the material, hence they are random in nature. The microcracks eventually coalesce and lead to the formation of a fatigue (macro-)crack, whose size is sufficient to neglect the aleatory nature of the material microstructure. This macro-crack then propagates first stably and finally unstably leading to failure.

The early studies on fatigue are mostly empirical and based on the data fitting of vast experimental campaigns [4]. In [5] Wöhler (1870) studies fatigue using experimental curves relating the maximum number of cycles that a component can undergo before failure, N_u , to the (constant) applied stress amplitude σ_a (Fig. 1a). This curve, named Wöhler or $S - N$ curve, is still used and is mathematically formalized by, e.g., the Basquin relationship

$$\sigma_a = AN_u^\beta, \quad (1)$$

where A and β are empirical coefficients that depend on the geometry and test setup. Wöhler's approach catches some characteristic features of fatigue such as the leading role of the load amplitude, the presence of an upper stress amplitude related to the monotonic strength of the material and the (possible) presence of a fatigue threshold. We divide here the Wöhler curve in three regions corresponding to (i) oligocyclic (OC), (ii) low-cycle (LC) and (iii) high-cycle (HC) fatigue (Fig. 1a). The OC region is related to high load levels, therefore N_u is rather limited, the material is largely damaged already after the first cycles and the stable crack propagation phase tends to disappear. In the LC region damage and fatigue processes compete, leading to a stable crack propagation phase whose extension is comparable to the nucleation and failure phases. In the HC region the fatigue life is dominated by the stable crack propagation phase. If the material features a fatigue threshold, this region asymptotically approaches an infinite fatigue life branch.

Palmgren (1924) [6] and Miner (1945) [7] introduce for the first time the concept of cumulative damage in the study of fatigue. Following the work of Wöhler, they postulate that, if there are k different stress amplitudes in a loading history, one cycle performed at σ_a^i ($1 \leq i \leq k$) gives a contribution to the overall damage equal to $\gamma_i = 1/N_u(\sigma_a^i)$ independently on the sequence of cycles. The following failure criterion¹ is then proposed

$$\sum_{i=1}^k n_{\sigma_a^i} \gamma_i = \sum_{i=1}^k \frac{n_{\sigma_a^i}}{N_u(\sigma_a^i)} = 1. \quad (2)$$

¹Note that in the original contribution [7] failure is intended as the onset of a crack.

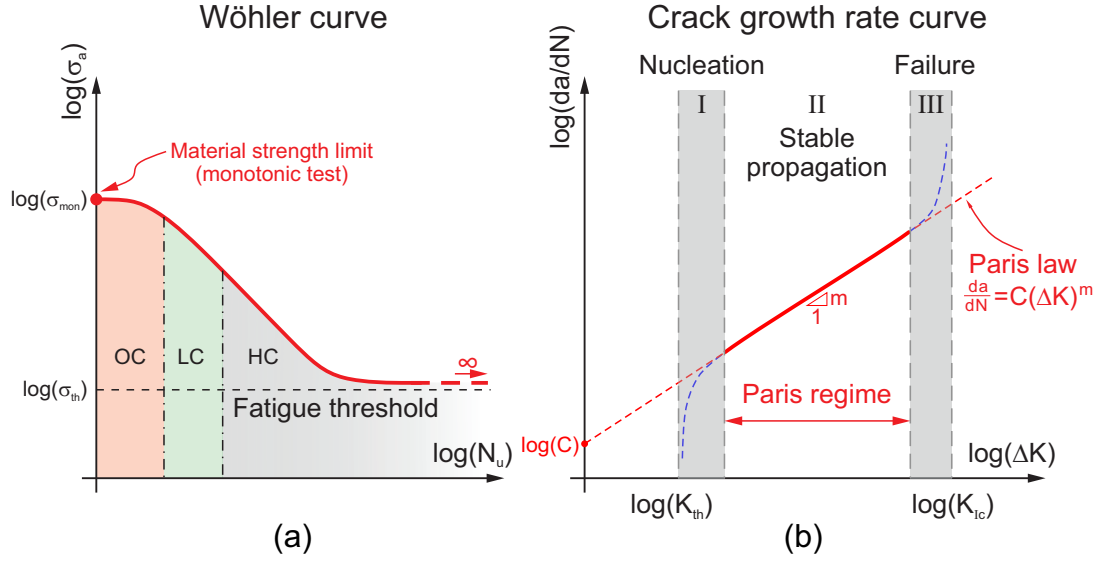


Fig. 1: (a) Wöhler or $S - N$ curve. (b) Crack growth rate curve and Paris law.

where $n_{\sigma_a^i}$ is the total number of cycles done at σ_a^i .

The formalization of the fracture mechanics theory of Griffith (1921) [8] radically changes the study of fatigue. Paris (1961) [9], after the work of Irwin (1957) [10], has the pioneering idea of proposing the stress intensity factor range in a single fatigue cycle ΔK as driving force for the fatigue growth of a crack with length a . The stress intensity factor summarizes locally at the crack tip the influences of the external loads, boundary conditions and geometry, making local an apparently structural problem. Fig. 1b shows an illustrative crack growth rate curve da/dN vs. ΔK in a bi-logarithmic scale obtained from constant amplitude cyclic fatigue tests. In general, this curve permits to distinguish three different regions related respectively to the crack nucleation (*I*), stable propagation (*II*) and unstable propagation (*III*). The extension of the stable propagation branch can vary depending on the severity of the applied load (i.e., OC, LC or HC regimes in Fig. 1a). Due to the microstructural-related nature of crack nucleation, the nucleation branch is usually affected by a high scatter. However, when a singularity in the component is present, e.g., a pre-existing notch, the scatter decreases and the crack nucleation and successive propagation can be assumed as nearly-deterministic.

Paris and Erdogan (1963) [11] proposed the following relationship, known as Paris law, to describe the stable propagation of a fatigue crack (red branch

of the curve in Fig. 1b)

$$\frac{da}{dN} = C\Delta K^m. \quad (3)$$

The two constants C and m need to be experimentally calibrated and are meant to be material parameters. Eq. 3 is valid only for low crack growth rate (i.e., $da/dN \leq 10^{-4}$ mm/cycle following [12, 13]), within the so-called Paris regime and is unable to reproduce the crack nucleation and failure phases (Fig. 1b). Trying to overcome its limits, Eq. 3 has been constantly improved and extended until reaching, today, the form of the widespread *NASGRO* equation [14], that reproduces many characteristic aspects of the fatigue behavior, such as the nucleation, propagation and failure phases, the crack closure effect [15], the presence of different cracking modes and the effect of the maximum load reached within the cycle [16] but at the cost of introducing up to 11 parameters [17].

The principal drawbacks related to the early approaches such as the Wöhler and Palmgren-Miner rules (and their extensions) are rooted in their empirical nature, that makes them hardly extendable to conditions different from the specific situation tested. Moreover, they focus only on failure and not on crack growth. Also, the Wöhler curve is limited to the cases of constant amplitude cycles. The Palmgren-Miner rule is valid only when the order of application of the cycles does not influence the results. This happens in some special cases reported in Appendix A or when the applied load is random. Conversely, the approaches based on Paris law are limited by the necessity of knowing ΔK which is, in general, a function of the crack length, geometry and boundary conditions. Analytical relationships exist only for few cases with very simple geometries and boundary conditions. In more general cases they can be found with numerical approaches such as the finite element method (FEM).

The numerical simulation of fatigue crack growth is much more flexible than the use of analytical methods but involves a double-fold challenge: on one hand we need a suitable way to represent the crack and, on the other hand, the latter should evolve as a result of fatigue for loads below the monotonic strength. The former issue is common to the monotonic case and the advantages and shortcomings of the available approaches are summarized, e.g., in [18]. Concerning the latter, here we limit ourselves to highlight the major pros and cons of each class of methods, while extensive reviews can be found in [19–21].

The FEM or the extended FEM (XFEM) can be used to numerically obtain the ΔK values to be used in Paris-like laws [17, 19, 20]. For some standard geometries, parameterized relationships based on best fitting proce-

dures are also available [22] and adopted by material testing guidelines such as [12, 13]. This approach is limited by the necessity of assuming an initial notch and needs criteria to determine the direction and shape evolution of the crack. Even more critical is the need to update the geometry of the problem when the crack front advances, which becomes extremely complex in 3-D [19]. This procedure is also hardly applicable to multiple cracks especially in case of merging/branching phenomena, complex geometries and/or loading conditions. Another family of approaches, including e.g. crystal plasticity and molecular dynamics models [23–25], describes the material behavior at a very small scale where the microstructure cannot be neglected. While these approaches contribute an important insight into the physics of the fatigue crack nucleation phenomena, their adoption for domains representative of real scale components is at the present stage unfeasible. Rather, they can be used to investigate the uncertainty in the fatigue crack nucleation phase as a result of the distribution of microstructural imperfections.

An issue common to all approaches is the calibration of the parameters. All the methods based on linear elastic analyses to obtain the ΔK values and many continuum damage or cohesive interface models use a Paris-like law and/or the Wöhler curve as input rather than obtaining them as output [19, 20, 26]. Other models are deemed to reproduce only a specific fatigue-related aspect disregarding the general behavior [24, 27]. Another limitation of some continuum damage and plasticity approaches [21, 28, 29] is the definition of evolution equations for the fatigue process that are often uncorrelated with the fracture mechanics or involve a large number of parameters with unclear physical meaning.

The variational phase-field approach to fracture [30, 31] is very attractive to model crack nucleation and propagation. It describes a steep but smooth transition from intact to fully cracked material states by means of an order parameter termed phase-field variable [18]. The approach can recover Griffith’s theory as a limit case in the Γ -convergence sense, and at the same time can be classified as a gradient damage approach [32]. The framework is very attractive because it can easily deal with complex crack patterns in 3-D with no need for remeshing nor for particular criteria to track the crack propagation. Boldrini et al. [33] proposed a phase-field model that couples the cracking behavior with the thermal and fatigue problem. The fatigue effect is introduced as an additional order parameter and its evolution is postulated under some restrictive conditions to preserve the thermodynamic consistency. Also, in [34, 35] the authors adopt the Ginzburg-Landau formalism to formulate a phase-field model accounting for fracture, visco-elasticity and environmental effects. Here, a fatigue potential is introduced to allow the degradation of the material under fatigue loadings. In both cases, no

evidence is given that the proposed model reproduces the major features of the fatigue behavior.

In general, a framework that is able to reproduce both the mechanics of monotonic fracture (comprising nucleation, propagation and failure) and the known features of the fatigue behavior including the Paris law, the Wöhler curve with the transition between oligo-, low- and high-cyclic fatigue and the Palmgren-Miner law is still missing.

In the present paper we propose a novel approach to model the fatigue behavior of brittle materials based on variational phase-field modeling of fracture. The first 1-D investigation has been reported in [36] and the existence of quasi-static evolutions with a vanishing viscosity approach studied in [37]. As in [36] we modify the free energy potential of the monotonic case introducing a suitable fatigue history variable and a fatigue degradation function that modifies the rate of the dissipated energy accounting for the fatigue loading history. The proposed approach aims at linking regularized monotonic fracture mechanics to fatigue crack growth establishing a framework suitable for any type of (brittle) materials. We are able to reproduce the major features of the fatigue behavior including the crack nucleation, stable and unstable propagation phases. Also, the Paris law and the Wöhler curve are recovered naturally, while the Palmgren-Miner rule and the monotonic behavior are encompassed as special cases.

The paper is structured as follows: the adopted phase-field model of brittle fracture is briefly summarized in Section 2 and extended to fatigue in Section 3. Sections 4 and 5 illustrate respectively the details of the numerical implementation and the numerical examples, while conclusions are drawn in Section 6.

2. Starting point: monotonic loading

In this section we briefly recall the phase-field model of brittle fracture under monotonic loading adopted as starting point [18, 31, 32, 38]. Isothermal conditions, negligible inertial effects and smooth loading in time are assumed. This allows to rely on the energetic principles of rate-independent systems [39], in the form of an *energy balance*, a *dissipation inequality* and a *stability criterion* applied to a properly defined set of energetic quantities. Also, the assumptions of small strains and of irreversibility for any dissipative process are assumed to hold.

2.1. Phase-field modeling of brittle fracture under monotonic loading

Consider a linear elastic D -dimensional body Ω susceptible of brittle fracture. The internal energy density is assumed as

$$W(\boldsymbol{\varepsilon}(\mathbf{u}), d, \nabla d) = \psi_{el}(\boldsymbol{\varepsilon}(\mathbf{u}), g(d)) + \varphi(d, \nabla d), \quad (4)$$

where $\psi_{el}(\boldsymbol{\varepsilon}(\mathbf{u}), g(d))$ is the stored elastic energy density and $\varphi(d, \nabla d)$ is the fracture energy density. Also, $\boldsymbol{\varepsilon}$ is the infinitesimal strain tensor related to the displacement field \mathbf{u} by $\boldsymbol{\varepsilon} = \nabla^s(\mathbf{u})$, ∇^s being the symmetric gradient operator, while d is the scalar phase-field parameter varying smoothly from 0 (sound material) to 1 (broken material). The *degradation function* $g(d)$ governs the transition of the mechanical behavior of the material from the sound to the cracked state, with

$$g(0) = 1, \quad g(1) = 0, \quad g'(d) \leq 0 \text{ for } 0 \leq d \leq 1. \quad (5)$$

The fracture energy density is written as [18, 31, 32]

$$\varphi(d, \nabla d) = \frac{G_c}{4c_w} \left(\frac{w(d)}{\ell} + \ell |\nabla d|^2 \right) \quad \text{with} \quad c_w = \int_0^1 \sqrt{w(\delta)} d\delta, \quad (6)$$

where ℓ is a regularization length, G_c is the fracture toughness of the material and $w(d)$ is termed *dissipation function*. In general, $w(d)$ must fulfill the following properties [40]

$$w(0) = 0, \quad w(1) = 1, \quad w'(d) \geq 0 \text{ for } 0 \leq d \leq 1. \quad (7)$$

Substituting Eq. 6 into Eq. 4 and integrating over Ω gives the free energy functional

$$E_\ell(\mathbf{u}, d) = \int_\Omega \psi_{el}(\boldsymbol{\varepsilon}(\mathbf{u}), g(d)) d\mathbf{x} + \frac{G_c}{4c_w} \int_\Omega \left(\frac{w(d)}{\ell} + \ell |\nabla d|^2 \right) d\mathbf{x}. \quad (8)$$

Γ -convergence results ensure that the global minima of E_ℓ in Eq. 8 converge to those of the unregularized functional as $\ell \rightarrow 0$ [30, 40, 41].

Applying the energy principles to Eq. 8, along with the irreversibility condition

$$\dot{d} \geq 0, \quad (9)$$

leads to the governing equations of the problem in terms of momentum balance and crack propagation conditions and respective boundary conditions (see sect. 3).

2.2. Degradation function and dissipation function

The degradation function describes the smooth degradation of the material behavior from sound to fully cracked state. Although alternatives are proposed in the literature [42–44], the present work is limited to the analysis of the well known relationship [18, 31, 38]

$$g(d) = (1 - d)^2. \quad (10)$$

The dissipation function rules the energy dissipation due to the formation of a new crack (Eq. 6). Here we adopt two widely used models [45]

1. **AT2 model:** originally proposed by Ambrosio and Tortorelli [41] and then adopted in [31] and many following works

$$w(d) = d^2 \quad \text{and} \quad c_w = \frac{1}{2}. \quad (11)$$

As $w'(d) = 0$, this model features a vanishing threshold for the onset of damage, leading to a material model without an initial linear elastic branch.

2. **AT1 model:** proposed in [32] with the aim of reproducing a constitutive behavior with an initial linear elastic branch. It reads

$$w(d) = d \quad \text{and} \quad c_w = \frac{2}{3}. \quad (12)$$

2.3. Decomposition of the elastic strain energy density

An additive decomposition of the undamaged elastic strain energy density into active and inactive parts is needed to describe the tension/compression asymmetry in the material behavior. The elastic strain energy density $\psi_{el}(\boldsymbol{\varepsilon}, g(d))$ is assumed as

$$\psi_{el}(\boldsymbol{\varepsilon}, g(d)) = g(d)\psi_{el,0}^+(\boldsymbol{\varepsilon}) + \psi_{el,0}^-(\boldsymbol{\varepsilon}) = \psi_{el}^+(\boldsymbol{\varepsilon}, d) + \psi_{el}^-(\boldsymbol{\varepsilon}), \quad (13)$$

where $\psi_{el,0}^+(\boldsymbol{\varepsilon})$ and $\psi_{el,0}^-(\boldsymbol{\varepsilon})$ are the active and inactive parts of the undamaged elastic strain energy density $\psi_{el,0}$. For an isotropic material $\psi_{el,0} = \psi_{el,0}^+ + \psi_{el,0}^- = \frac{1}{2}\lambda \text{tr}^2(\boldsymbol{\varepsilon}) + \mu \text{tr}(\boldsymbol{\varepsilon})^2$, λ and μ being the Lamé constants. Accordingly, the stored elastic strain energy density of a damaged material is split into an active part $\psi_{el}^+(\boldsymbol{\varepsilon}, g(d))$ that is degraded and an inactive part $\psi_{el}^-(\boldsymbol{\varepsilon})$ not affected by the phase field parameter. Although other options are available [44, 46, 47], the present work adopts the following choices:

1. **Isotropic model**: proposed in [31], it features the degradation of the whole elastic strain energy density. Hence, it lets the fracture propagate also in compressed regions [48].
2. **Volumetric/deviatoric split**: proposed in [48] to overcome the drawbacks of the isotropic model. The degradation function affects only the energy density related to the deviatoric and to the positive volumetric part of the strain tensor.
3. **Spectral split**: proposed in [38], it distinguishes between degraded and undegraded parts of the energy using the spectral decomposition of the strain tensor.
4. **No-tension split**: proposed in [49], it degrades the energy related to the positive-definite symmetric part of the strain tensor leaving undegraded the remaining part.

2.4. Homogeneous 1-D solution of the phase-field problem

Studying analytically the homogeneous 1-D solution [32], it is possible to compute the peak stress σ_y and the corresponding strain ε_y as functions of the Young's modulus E , the regularization length ℓ and the fracture toughness G_c as follows

$$\sigma_y^{AT2} = \frac{9}{16} \sqrt{\frac{EG_c}{3\ell}}, \quad \varepsilon_y^{AT2} = \sqrt{\frac{G_c}{3\ell E}}, \quad (14)$$

for the AT2 model and

$$\sigma_y^{AT1} = \sqrt{\frac{3EG_c}{8\ell}}, \quad \varepsilon_y^{AT1} = \sqrt{\frac{3G_c}{8\ell E}}, \quad (15)$$

for the AT1 model.

3. Extension to fatigue behavior

In this section the phase-field modeling approach to brittle fracture in section 2 is extended to fatigue.

3.1. Energetic quantities

To introduce the fatigue effects, we propose to modify the fracture energy density similarly to [36] as follows

$$\begin{aligned} \varphi_F(d, \nabla d | \bar{\alpha}([0, t])) &= \int_0^t f(\bar{\alpha}(\tau)) \dot{\varphi}(d, \nabla d) d\tau \\ &= \int_0^t f(\bar{\alpha}(\tau)) \left(\frac{\partial \varphi}{\partial d} \dot{d} + \frac{\partial \varphi}{\partial \nabla d} \cdot \nabla \dot{d} \right) d\tau, \end{aligned} \quad (16)$$

where t is the pseudo-time, $\bar{\alpha}(t)$ is a properly defined cumulated history variable acting in Eq. 16 as a parameter, while $f(\bar{\alpha}(t))$ is a *fatigue degradation function*.

Remark 1 (Dissipated energy). *In this framework the dissipated energy is a process dependent quantity and no longer a state function.*

Remark 2 (Choice of $\bar{\alpha}(t)$). *The history variable $\bar{\alpha}(t)$ is not yet defined at this stage. It can be taken as a cumulation of any scalar quantity α which can exhaustively describe the fatigue history experienced by the material so that*

$$\dot{\bar{\alpha}}(t) = |\dot{\alpha}| \geq 0. \quad (17)$$

Remark 3 (Dissipation). *The dissipation is still related only to the damage variable, because $\bar{\alpha}(t)$ acts in Eq. 16 merely as a parameter that tunes the dissipation rate accounting for the load history experienced by the material. In other words, while the effective dissipative work is still due to the evolution of the phase-field variable and its gradient, the function $f(\bar{\alpha}(t))$ effectively modulates the fracture toughness as a function of the “mileage” as expressed by the variable $\bar{\alpha}(t)$.*

Remark 4 (Support of the phase field). *Substituting Eq. 6 into Eq. 16 it is*

$$\dot{\varphi}_F(d, \nabla d | \bar{\alpha}([0, t])) = f(\bar{\alpha}(t)) \frac{G_c}{4c_w} \left(\frac{w'(d)}{\ell} \dot{d} + 2\ell \nabla d \cdot \nabla \dot{d} \right), \quad (18)$$

where it is evident that the function $f(\bar{\alpha}(t))$ affects both local and gradient terms of the dissipative power. This choice ensures that the support of the phase-field variable remains the same as in the monotonic case [38].

The function $f(\bar{\alpha}(t))$ is assumed to have the following properties

$$f(\bar{\alpha} \leq \alpha_T) = 1, \quad f(\bar{\alpha} > \alpha_T) \in [0, 1], \quad f'(\bar{\alpha}) \leq 0 \text{ for } 0 \leq f(\bar{\alpha}) < 1, \quad (19)$$

where α_T is a threshold controlling when the fatigue effect is triggered.

The total internal energy density assumes now the form

$$\begin{aligned} W(\boldsymbol{\varepsilon}(\mathbf{u}), d, \nabla d | \bar{\alpha}) &= \psi_{el}(\boldsymbol{\varepsilon}(\mathbf{u}), g(d)) + \\ &+ \int_0^t f(\bar{\alpha}(\tau)) \frac{G_c}{4c_w} \left(\frac{w'(d)}{\ell} \dot{d} + 2\ell \nabla d \cdot \nabla \dot{d} \right) d\tau, \end{aligned} \quad (20)$$

thus becoming (time-)history-dependent. To circumvent this dependency the energetic principles are here applied to the total internal power density

$$\begin{aligned} \dot{W}(\boldsymbol{\varepsilon}(\mathbf{u}), d, \nabla d | \bar{\alpha}) &= \boldsymbol{\sigma} : \dot{\boldsymbol{\varepsilon}}(\mathbf{u}) + \frac{\partial \psi_{el}}{\partial d} \dot{d} + \\ &+ f(\bar{\alpha}(t)) \frac{G_c}{4c_w} \left(\frac{w'(d)}{\ell} \dot{d} + 2\ell \nabla d \cdot \nabla \dot{d} \right). \end{aligned} \quad (21)$$

where the Cauchy stress tensor $\boldsymbol{\sigma}$ is introduced as

$$\boldsymbol{\sigma} = \frac{\partial \psi_{el}}{\partial \boldsymbol{\varepsilon}}. \quad (22)$$

3.2. Governing equations

Applying now the energetic principles for a rate-independent system in rate form it is possible to determine the governing equations of the problem. The solution (\mathbf{u}, d) satisfies the energy balance principle if the following condition holds

$$\int_{\Omega} \dot{W}(\boldsymbol{\varepsilon}(\mathbf{u}), d, \nabla d | \bar{\alpha}) d\mathbf{x} - \dot{\mathcal{L}}(\mathbf{u}) = 0. \quad (23)$$

Here $\dot{\mathcal{L}}(\mathbf{u})$ is the external power, given by

$$\dot{\mathcal{L}}(\mathbf{u}) = \int_{\partial\Omega_N} \mathbf{t}_n \cdot \dot{\mathbf{u}} dA + \int_{\Omega} \mathbf{b} \cdot \dot{\mathbf{u}} d\mathbf{x}, \quad (24)$$

where \mathbf{t}_n are the external tractions per unit area dA with outward unit normal \mathbf{n} applied at the Neumann boundary $\partial\Omega_N$ and \mathbf{b} are the body forces. By means of Eqs. 21 and 24, Eq. 23 becomes

$$\begin{aligned} \int_{\Omega} \boldsymbol{\sigma} : \dot{\boldsymbol{\varepsilon}}(\mathbf{u}) + \frac{\partial \psi_{el}}{\partial d} \dot{d} + f(\bar{\alpha}) \frac{G_c}{4c_w} \left(\frac{w'(d)}{\ell} \dot{d} + 2\ell \nabla d \cdot \nabla \dot{d} \right) d\mathbf{x} + \\ - \int_{\partial\Omega_N} \mathbf{t}_n \cdot \dot{\mathbf{u}} da - \int_{\Omega} \mathbf{b} \cdot \dot{\mathbf{u}} d\mathbf{x} = 0. \end{aligned} \quad (25)$$

Eq. 25 can be integrated by parts giving the following form of the energy

balance

$$\begin{aligned}
& \int_{\Omega} -(\operatorname{div} \boldsymbol{\sigma} + \mathbf{b}) \cdot \dot{\mathbf{u}} \, d\mathbf{x} + \\
& + \int_{\Omega} \left\{ \frac{\partial \psi_{el}}{\partial d} - \frac{G_c}{2c_w} \ell \left[f(\bar{\alpha}) \left(\Delta d - \frac{w'(d)}{2\ell^2} \right) + \nabla f(\bar{\alpha}) \cdot \nabla d \right] \right\} \dot{d} \, d\mathbf{x} + \quad (26) \\
& + \int_{\partial\Omega} (\boldsymbol{\sigma} \cdot \mathbf{n} - \mathbf{t}_n) \cdot \dot{\mathbf{u}} \, dA + \frac{G_c \ell}{2c_w} \int_{\partial\Omega} f(\bar{\alpha}) \nabla d \cdot \mathbf{n} \dot{d} \, dA = 0,
\end{aligned}$$

The first-order stability principle in rate form states that the solution (\mathbf{u}, d) is stable if for any possible admissible test velocities $(\dot{\mathbf{u}}, \dot{d})$ it satisfies

$$\begin{aligned}
& \int_{\Omega} -(\operatorname{div} \boldsymbol{\sigma} + \mathbf{b}) \cdot \dot{\mathbf{u}} \, d\mathbf{x} + \\
& + \int_{\Omega} \left[f(\bar{\alpha}) \frac{G_c}{4c_w} \frac{w'(d)}{\ell} + \frac{\partial \psi_{el}}{\partial d} - \operatorname{div} \left(f(\bar{\alpha}) \frac{G_c}{2c_w} \ell \nabla d \right) \right] \dot{d} \, d\mathbf{x} + \quad (27) \\
& + \int_{\partial\Omega} (\boldsymbol{\sigma} \cdot \mathbf{n} - \mathbf{t}_n) \cdot \dot{\mathbf{u}} \, dA + \int_{\partial\Omega} f(\bar{\alpha}) \frac{G_c}{2c_w} \ell \nabla d \cdot \mathbf{n} \dot{d} \, dA \geq 0.
\end{aligned}$$

Note that the admissible test velocity for d must satisfy the irreversibility condition Eq. 9.

Using standard arguments of variational calculus, Eq. 27 leads to the following local equilibrium equation and Neumann boundary conditions for the mechanical problem

$$\operatorname{div} \boldsymbol{\sigma} + \mathbf{b} = \mathbf{0} \quad \text{in } \Omega, \quad (28a)$$

$$\boldsymbol{\sigma} \cdot \mathbf{n} = \mathbf{t}_n \quad \text{on } \partial\Omega_N. \quad (28b)$$

(Note that \mathbf{u} must a priori satisfy the Dirichlet boundary condition $\mathbf{u} = \bar{\mathbf{u}}$ on the Dirichlet boundary $\partial\Omega_D$.) For the phase-field problem the following inequalities are obtained

$$\frac{\partial \psi_{el}}{\partial d} - \frac{G_c \ell}{2c_w} \left[f(\bar{\alpha}) \left(\Delta d - \frac{w'(d)}{2\ell^2} \right) + \nabla f(\bar{\alpha}) \cdot \nabla d \right] \geq 0 \quad \text{in } \Omega, \quad (29a)$$

$$\frac{G_c \ell}{2c_w} f(\bar{\alpha}) \nabla d \cdot \mathbf{n} \geq 0 \Rightarrow \nabla d \cdot \mathbf{n} \geq 0 \quad \text{on } \partial\Omega. \quad (29b)$$

From Eq. 26 combined with Eq. 28 the energy balance reduces to

$$\int_{\Omega} \left\{ \frac{\partial \psi_{el}}{\partial d} - \frac{G_c}{2c_w} \ell \left[f(\bar{\alpha}) \left(\Delta d - \frac{w'(d)}{2\ell^2} \right) + \nabla f(\bar{\alpha}) \cdot \nabla d \right] \right\} \dot{d} d\mathbf{x} + \frac{G_c \ell}{2c_w} \int_{\partial\Omega} f(\bar{\alpha}) \nabla d \cdot \mathbf{n} \dot{d} dA = 0. \quad (30)$$

Being $\dot{d} \geq 0$ from Eq. 9 and accounting for the inequalities in Eq. 29, the left hand side of Eq. 30 is the sum of two non-negative terms. Therefore, each term must vanish, which leads to the following consistency conditions

$$\left\{ \frac{\partial \psi_{el}}{\partial d} - \frac{G_c}{2c_w} \ell \left[f(\bar{\alpha}) \left(\Delta d - \frac{w'(d)}{2\ell^2} \right) + \nabla f(\bar{\alpha}) \cdot \nabla d \right] \right\} \dot{d} = 0 \quad \text{in } \Omega. \quad (31a)$$

$$(\nabla d \cdot \mathbf{n}) \dot{d} = 0 \quad \text{on } \partial\Omega. \quad (31b)$$

Eqs. 29a, 9 and 31a thus constitute the well-known Karush-Kuhn-Tucker (*KKT*) conditions which rule the evolution of the phase-field variable d .

The Clausius-Duhem dissipation inequality states that the following condition on the dissipation \mathcal{D} holds

$$\mathcal{D} = \int_{\Omega} W(\boldsymbol{\varepsilon}(\mathbf{u}), d, \nabla d | \bar{\alpha}) - \psi_{el}(\boldsymbol{\varepsilon}(\mathbf{u}), g(d)) d\mathbf{x} \geq 0, \quad (32)$$

or in rate form

$$\dot{\mathcal{D}} = \int_{\Omega} f(\bar{\alpha}) \frac{G_c}{2c_w} \left(\frac{w'(d)}{2\ell} \dot{d} + \ell \nabla d \cdot \nabla \dot{d} \right) d\mathbf{x} \geq 0, \quad (33)$$

where Eq. 21 is accounted for. Comparing Eq. 33 with Eq. 25 one has

$$\dot{\mathcal{D}} = \int_{\Omega} -\frac{\partial \psi_{el}}{\partial d} \dot{d} d\mathbf{x} \geq 0, \quad (34)$$

which holds since $\dot{d} \geq 0$ (Eq. 9) and $\frac{\partial \psi_{el}}{\partial d} \leq 0$ from Eq. 5.

3.3. Cumulated history variable

As already outlined in sect. 3.1, $\bar{\alpha}$ is a cumulated variable which quantifies the fatigue effects already experienced by the material.

Two cumulated variables are proposed in the following

1. Mean load independent: for materials whose fatigue life is not affected by the mean load of a cycle. It reads

$$\bar{\alpha}(\mathbf{x}, t) = \int_0^t H(\alpha \dot{\alpha}) |\dot{\alpha}| d\tau, \quad (35)$$

where $H(\alpha \dot{\alpha})$ the Heaviside function, defined as $H(\alpha \dot{\alpha}) = 1$ if $\alpha \dot{\alpha} \geq 0$ (loading) and $H(\alpha \dot{\alpha}) = 0$ otherwise (unloading).

2. Mean load dependent: the model can be enriched by introducing a history variable that weighs differently the rate of the cumulated variable depending on the load level achieved as

$$\bar{\alpha}(\mathbf{x}, t) = \frac{1}{\alpha_N} \int_0^t H(\alpha \dot{\alpha}) \alpha \dot{\alpha} d\tau, \quad (36)$$

where α_N is a normalization parameter needed to achieve dimensional consistency.

3.4. Fatigue degradation function

The fatigue degradation function $f(\bar{\alpha}(t))$ describes how fatigue effectively reduces the fracture toughness of the material. The following two fatigue degradation functions are considered here [36]

$$f(\bar{\alpha}(t)) = \begin{cases} 1 & \text{if } \bar{\alpha}(t) \leq \alpha_T \\ \left(\frac{2\alpha_T}{\bar{\alpha}(t) + \alpha_T} \right)^2 & \text{if } \bar{\alpha}(t) \geq \alpha_T, \end{cases} \quad (37)$$

and

$$f(\bar{\alpha}(t)) = \begin{cases} 1 & \text{if } \bar{\alpha}(t) \leq \alpha_T \\ \left[1 - \kappa \log \left(\frac{\bar{\alpha}(t)}{\alpha_T} \right) \right]^2 & \text{if } \alpha_T \leq \bar{\alpha}(t) \leq \alpha_T 10^{1/\kappa} \\ 0 & \text{if } \bar{\alpha}(t) \geq \alpha_T 10^{1/\kappa} \end{cases} \quad (38)$$

where κ is a material parameter. The difference between Eqs. 37 and 38 is that the former (Fig. 2a) delivers an asymptotically vanishing value while the latter (Fig. 2b) vanishes for a finite value of $\bar{\alpha}(t)$. Also, the slope of the logarithmic function Eq. 38 can be tuned by varying κ as shown in Fig. 2b, giving a further degree of freedom when simulating real material behaviors.

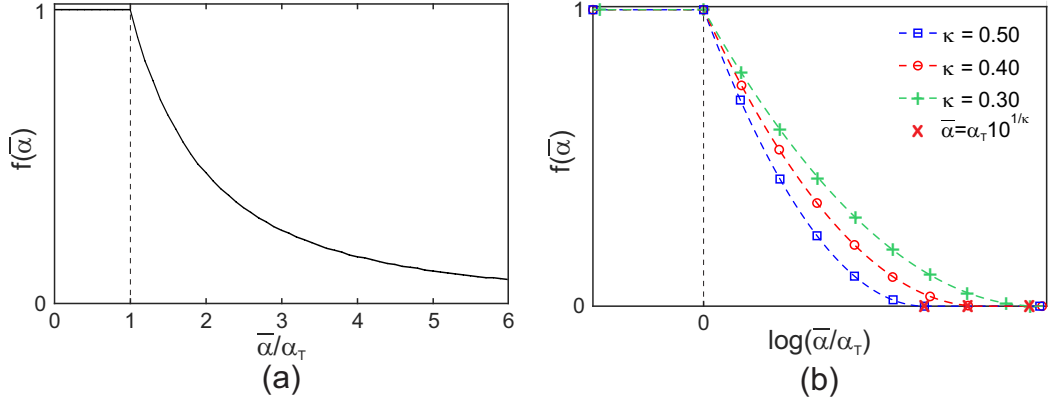


Fig. 2: Fatigue degradation function: (a) asymptotic and (b) logarithmic for different values of κ .

3.5. Choice of α

Concerning the fatigue history variable, in [36] it is assumed that the fatigue effects are driven by the strain, namely $\alpha = \varepsilon$ (in 1-D), which could be extended to 2- or 3-D by taking $\alpha = \|\boldsymbol{\varepsilon}\|$. Although proven to be effective in 1-D, this solution gives rise to mesh-dependency issues in a multi-dimensional framework as illustrated in sect. 5.1. Due to the energetic nature of the adopted modeling framework, it seems natural to account for the active part of the elastic strain energy density, i.e. $\alpha = \psi_{el}^+(\boldsymbol{\varepsilon}, d)$. Also, the fatigue effects are cumulated only during the loading phase [36, 50], defined as $\dot{\psi}_{el}^+ \geq 0$.

3.6. Summary

The governing equations and needed parameters of the proposed modeling framework are summarized in Tab. 1 where $\mathbb{C}^+(\lambda, \nu)$ and $\mathbb{C}^-(\lambda, \nu)$ are the constitutive elastic tensors related to the active and inactive parts of the elastic strain energy density.

4. Numerical implementation

To find the numerical solution, the mechanical and phase-field problems are written in weak form and, once discretized using linear finite elements and recasted in incremental form, they are solved using a staggered approach [38]. The convergence of the solution is ensured controlling the residual as proposed in [18]. As in [38], the crack irreversibility condition is enforced introducing the history variable

$$\mathcal{H} = \max_{\tau \in [0, t]} \psi_{el,0}^+(\boldsymbol{\varepsilon}(\mathbf{x}, \tau)). \quad (40)$$

Balance of momentum	
Equilibrium equation	$\operatorname{div} \{ [g(d)\mathbb{C}^+(\lambda, \nu) + \mathbb{C}^-(\lambda, \nu)] : \boldsymbol{\varepsilon} \} + \mathbf{b} = \mathbf{0} \quad \text{in } \Omega,$
Boundary conditions	$\boldsymbol{\sigma} \cdot \mathbf{n} = \mathbf{t}_n \quad \text{on } \partial\Omega_N,$ $\mathbf{u} = \bar{\mathbf{u}} \quad \text{on } \partial\Omega_D,$
Degradation function	$g(d) = (1 - d)^2$
Parameters	$\lambda, \nu \rightarrow \mathbb{C}^+(\lambda, \nu), \mathbb{C}^-(\lambda, \nu)$
Phase-field evolution	
KKT conditions	$\begin{cases} \frac{\partial \psi_{el}}{\partial d} - \frac{G_c}{2c_w} \ell \left[f(\bar{\alpha}) \left(\Delta d - \frac{w'(d)}{2\ell^2} \right) + \nabla f(\bar{\alpha}) \cdot \nabla d \right] \geq 0, \\ \dot{d} \geq 0, \\ \left\{ -\frac{\partial \psi_{el}}{\partial d} + \frac{G_c}{2c_w} \ell \left[f(\bar{\alpha}) \left(\Delta d - \frac{w'(d)}{2\ell^2} \right) + \nabla f(\bar{\alpha}) \cdot \nabla d \right] \right\} \dot{d} = 0. \end{cases}$
Boundary conditions	$\nabla d \cdot \mathbf{n} = 0 \quad \text{on } \partial\Omega$
Dissipation function	$w(d) = d^2 \quad (\text{AT2}) \quad \text{or} \quad w(d) = d \quad (\text{AT1})$
Parameters	G_c, ℓ
Fatigue	
History variable	$\dot{\bar{\alpha}} = H(\dot{\psi}_{el}^+) \dot{\psi}_{el}^+ \quad (\text{No mean load eff.})$ $\dot{\bar{\alpha}} = \frac{1}{\alpha_N} H(\dot{\psi}_{el}^+) \dot{\psi}_{el}^+ \dot{\psi}_{el}^+ \quad (\text{Mean load eff.})^\dagger$
Fatigue degradation function	$f(\bar{\alpha}(t)) = \begin{cases} 1 & \text{if } \bar{\alpha}(t) \leq \alpha_T \\ \left(\frac{2\alpha_T}{\bar{\alpha}(t) + \alpha_T} \right)^2 & \text{if } \bar{\alpha}(t) \geq \alpha_T, \end{cases} \quad (\text{Asymptotic})$ $f(\bar{\alpha}(t)) = \begin{cases} 1 & \text{if } \bar{\alpha}(t) \leq \alpha_T \\ \left[1 - \kappa \log \left(\frac{\bar{\alpha}(t)}{\alpha_T} \right) \right]^2 & \text{if } \alpha_T \leq \bar{\alpha}(t) \leq \alpha_T 10^{1/\kappa} \\ 0 & \text{if } \bar{\alpha}(t) \geq \alpha_T 10^{1/\kappa} \end{cases} \quad (\text{Logarithmic})^\square$
Parameters	$\alpha_T, \alpha_N \quad (\text{only for } \dagger), \kappa \quad (\text{only for } \square)$

Tab. 1: Governing equations and parameters.

The alternative approaches are discussed in [51].

4.1. Time integration

Within the time discretized setting, the updated value of the fatigue history variable reads

$$\bar{\alpha}_{n+1} = \bar{\alpha}_n + \int_{t_n}^{t_{n+1}} \dot{\bar{\alpha}} d\tau = \bar{\alpha}_n + \Delta\bar{\alpha}, \quad (41)$$

where the subscripts n and $n+1$ refer to the instants $t = t_n$ and $t = t_{n+1}$, respectively, $\Delta t = t_{n+1} - t_n$ and $\Delta\bar{\alpha}$ is approximated as

$$\Delta\bar{\alpha} = |\alpha_{n+1} - \alpha_n| H\left(\frac{\alpha_{n+1} - \alpha_n}{\Delta t}\right), \quad (42)$$

or

$$\Delta\bar{\alpha} = \frac{(\alpha_{n+1} - \alpha_n)}{\alpha_N} \left(\frac{\alpha_{n+1} + \alpha_n}{2}\right) H\left(\frac{\alpha_{n+1} - \alpha_n}{\Delta t}\right), \quad (43)$$

respectively if the mean load independent (Eq. 35) or dependent (Eq. 36) accumulation function is used.

5. Numerical examples

In this section some numerical experiments are presented and discussed. On one hand we illustrate the major features of the proposed framework and on the other hand we compare qualitatively and quantitatively the numerical results with the known results about fatigue.

In the remainder of this paper and if not specified otherwise, the AT2 model (Eq. 11), the mean load independent accumulation function (Eq. 35) and the asymptotic fatigue degradation function (Eq. 37) are used, while a spatial discretization $h = \frac{\ell}{5}$ is adopted within the region of the specimen where the crack propagation is expected. Furthermore, when calculating the crack length, the origin is taken at the pre-existing notch tip and we consider completely cracked any point where $d \geq 0.95$.

The fatigue-related quantities α_T and α_N are meant to be material parameters to be determined on an experimental basis. However, the comparison with experimental results is out of the scope of the present work. Hence, it is here assumed that

$$\alpha_T = \alpha_N = \frac{1}{2} \varepsilon_y^{AT2} E \varepsilon_y^{AT2}, \quad (44)$$

where ε_y^{AT2} is defined in Eq. 14. This choice is made to permit a proper comparison between the results as well as to highlight that no fine tuning of the parameter is performed.

5.1. Single-edge notched test

To evaluate the performance of the model, the widely investigated single-edge notched specimen [18, 38, 44] is tested. Pure tensile and shear conditions are considered and the corresponding numerical monotonic loading curves along with the geometry and boundary conditions used are presented in Fig. 3. The material parameters adopted are $E = 210\text{GPa}$, $\nu = 0.3$, $G_c = 2.70\text{N/mm}$, $\alpha_T = \alpha_N = 5.625 \cdot 10^1\text{N/mm}^2$ and $\ell = 0.004\text{mm}$. All the simulations are performed in plane strain conditions and displacement control.

Note that the maximum monotonic load obtained using the present framework is slightly lower than that obtained with the standard formulation of sect. 2 if the same elastic and phase-field parameters are used. This happens because already during the monotonic loading phase a certain effective degradation of G_c takes place. This only apparent issue can be solved by a proper parameter calibration. Also, some jumps in the load-displacement curve due to locally induced snap-back instabilities are observed in the post-peak phase of the shear test (Fig. 3b). The same issue is observed also with the standard monotonic approach, although to a different extent. This difference can be ascribed to the effect of $f(\bar{\alpha})$ that degrades the fracture toughness of the portion of material ahead of the crack tip, which leads to phases of abrupt crack propagation.

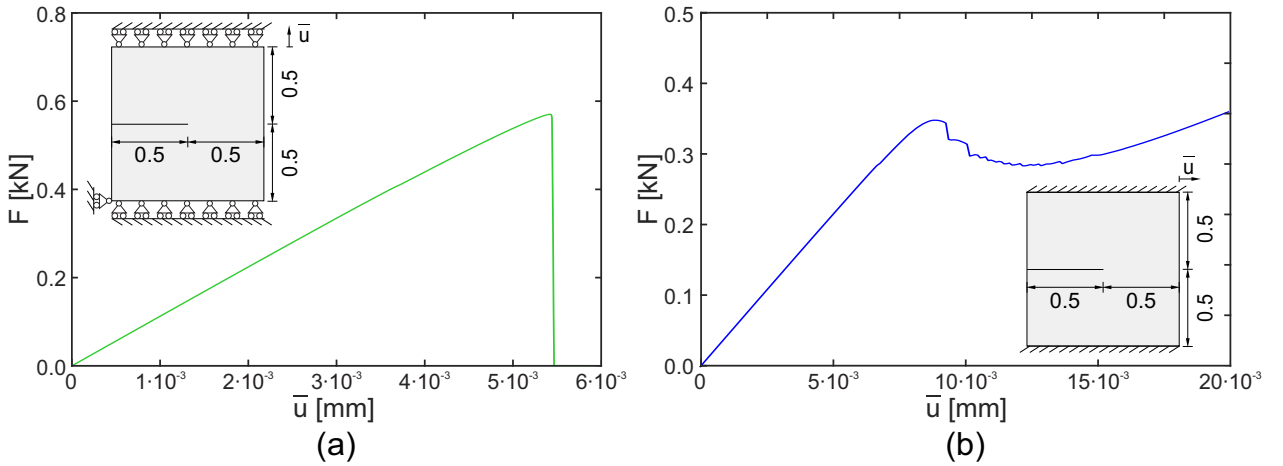


Fig. 3: Geometry and boundary conditions of the single edge notched specimen: (a) tensile and (b) shear test.

To investigate the effect of the adopted tension-compression split (sect. 2.3), a cyclic tensile test is performed. A symmetric cyclic load is applied with $\Delta\bar{u} = 4 \cdot 10^{-3}\text{mm}$ (Fig. 4a). The results in terms of the accumulation of the

fatigue history variable $\bar{\alpha}$ vs. the number of cycles N (fatigue life curves) illustrate that the isotropic model [31] leads to the evolution of α during all the loading phases, regardless of whether the induced stress state is positive, i.e. tension (branch AB in Fig. 4a), or negative, i.e. compression (branch CD in Fig. 4a). The consequence is an unphysical behavior for both fracture and fatigue, since a crack is meant to propagate under tension [38, 48, 49] and it was proven by Elber [15] that, in case of negligible plasticity, the detrimental fatigue effect should be attributed to tensile stress states only.

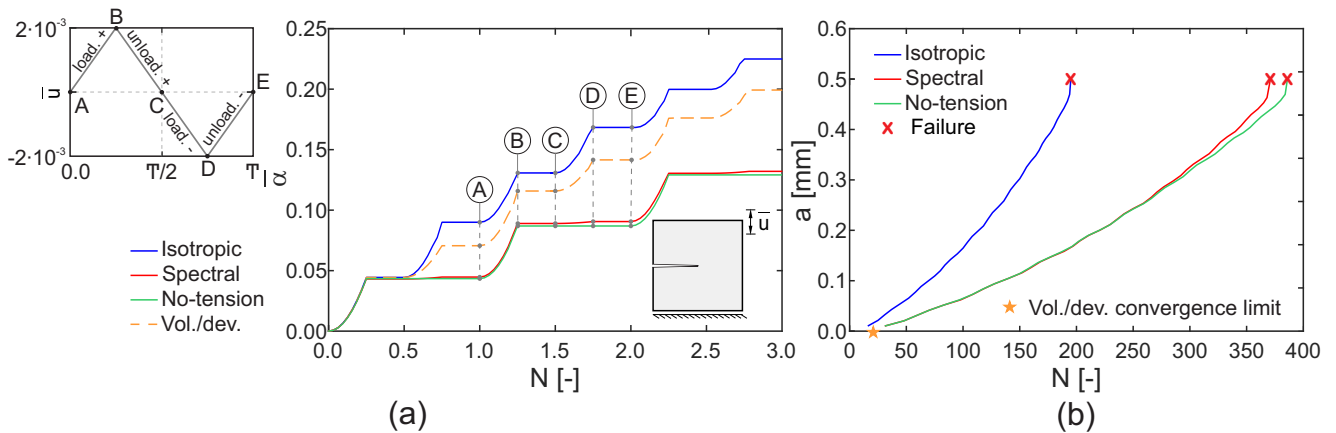


Fig. 4: Accumulation of the fatigue history variable α for few illustrative cycles and (b) fatigue life curves up to failure for different splits.

Adopting the volumetric/deviatoric split [48] leads to loss of iterative convergence after the onset of the crack (Fig. 4b). This is due to a pathological behavior of the split itself that leaves undamaged only the compressive volumetric strain energy and thus leads to a fluid-like behavior. For this reason the volumetric/deviatoric split is no longer considered in the following. The spectral [38] and no-tension [49] splits distinguish between tension and compression loading phases and behave similarly, the only difference being the amount of energy dissipated during the negative loading phases and hence the evolution of $\bar{\alpha}$. In particular for the case analyzed here, the spectral split degrades a limited fraction of the deviatoric energy related to the positive principal strain, while the no-tension split does not degrade energy. This leads to negligible differences in the fatigue life, whereas using the isotropic model the fatigue life is decreased by half being the degradation double (Fig. 4b). Note that, for all models, the accumulation of the fatigue history variable $\bar{\alpha}$ during unloading (branches BC and DE in Fig. 4a) is prevented by the loading-unloading condition of Eqs. 35 and 36.

Following the obtained results, in the remaining of the paper the spectral

split will be used if not differently specified.

The convergence of the simulations with the mesh size h using either $\alpha = \|\boldsymbol{\varepsilon}\|$ or $\alpha = \psi_{el}^+$ is evaluated in Figs. 5a,b. As mentioned earlier, the former choice leads to a strong mesh dependence (Fig. 5a) due to the strain field singularity at the crack tip. Conversely, with $\alpha = \psi_{el}^+$ convergence is already reached for $h = \ell/3$ (Fig. 5b). The sensitivity of the results to the length scale parameter ℓ is investigated in Fig. 5c. Here we can observe that, in agreement with the results in [45], only marginal differences are visible varying the length scale from $6 \cdot 10^{-3}$ mm to $4 \cdot 10^{-3}$ mm. Fig. 5d illustrates the results of the simulations for different pseudo-time discretizations of the load cycle ABCDE of Fig. 4a, demonstrating that convergence is reached already using 8 load steps per cycle.

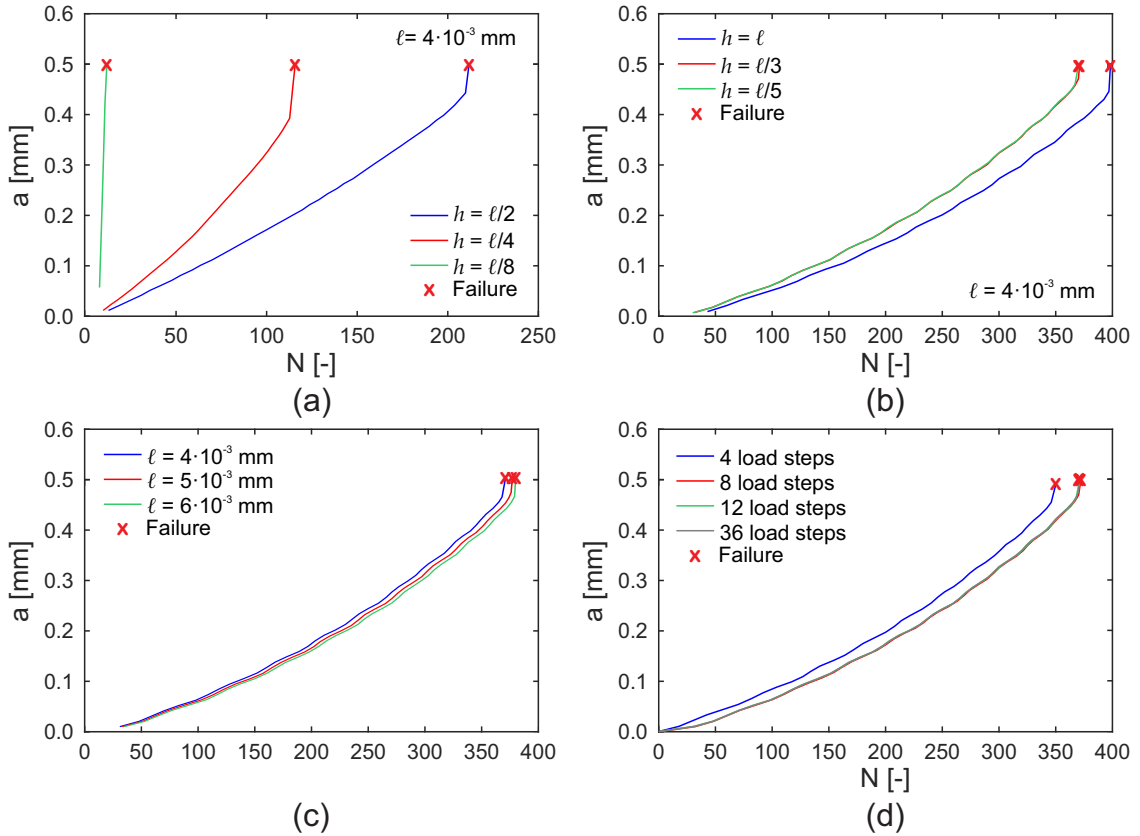


Fig. 5: Crack length a vs. number of cycles N : convergence study for different mesh sizes h adopting (a) $\alpha = \|\boldsymbol{\varepsilon}\|$ or (b) $\alpha = \psi_{el}^+$, (c) effect of the length scale parameter ℓ and (d) effect of the cycle (i.e., pseudo-time) discretization.

Fig. 6a shows the substantial role of the load range on the fatigue life as predicted by the proposed model. Increasing the load range leads to a

reduction of number of cycles to both crack nucleation N_y and failure N_u . Interestingly, upon normalizing the result by N_u all curves cluster together, meaning that the fatigue process depends mainly on how far the crack has propagated rather than on the load history. This is due to the specific displacement controlled boundary condition of Fig. 3a, that makes the product between the applied force and the shape factor of the stress intensity factor range roughly constant (see Appendix A for a detailed justification).

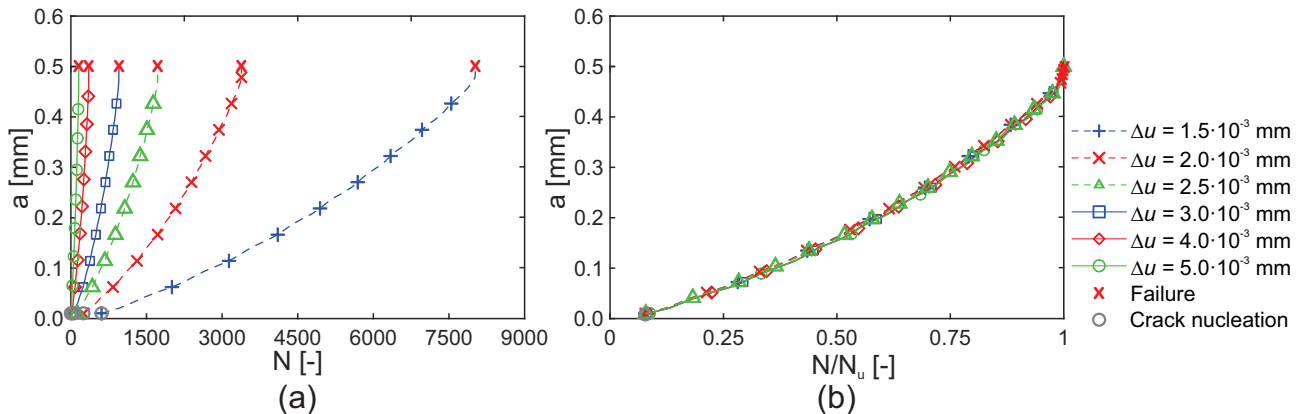


Fig. 6: Fatigue life curves for different applied displacement ranges Δu (a) N vs. a and (b) normalized N/N_u vs. a .

The aforementioned condition is in agreement with the assumptions underlying Eq. 2, suggesting thus that the Palmgren-Miner criterion can be approximately reproduced by the present approach for the special case of the displacement controlled tests. To prove this, two tests are performed where the cyclic load is constituted by three blocks of five constant amplitude cycles as in Fig. 7a. The ranges of the applied displacement are $\Delta\bar{u}_1 = 3.0 \cdot 10^{-3} \text{ mm}$ - $\Delta\bar{u}_2 = 4.0 \cdot 10^{-3} \text{ mm}$ - $\Delta\bar{u}_3 = 5.0 \cdot 10^{-3} \text{ mm}$ for the test labeled H and $\Delta\bar{u}_1 = 1.5 \cdot 10^{-3} \text{ mm}$ - $\Delta\bar{u}_2 = 2.0 \cdot 10^{-3} \text{ mm}$ - $\Delta\bar{u}_3 = 2.5 \cdot 10^{-3} \text{ mm}$ for the test labeled L. Figs. 7b,c present the cumulated Palmgren-Miner damage $D = \sum_{i=1}^N \gamma_i$ respectively for crack nucleation D_y and failure D_u of the specimen. Both approach the unit value with deviations around 10%. As highlighted in Appendix A, this is one of the few special cases where the assumptions of the Palmgren-Miner rule are approximately satisfied for a crack growth ruled by Paris law.

Fig. 8a compares the fatigue life curves obtained adopting the AT2 and AT1 models. For a proper comparison between the two models, E and G_c are kept constant while the regularization length ℓ is determined either by imposing $\sigma_y^{AT2} = \sigma_y^{AT1}$ or $\varepsilon_y^{AT2} = \varepsilon_y^{AT1}$ following Eqs. 14 and 15. The difference in terms of fatigue life N_u is limited and ranges between 10% and 15%.

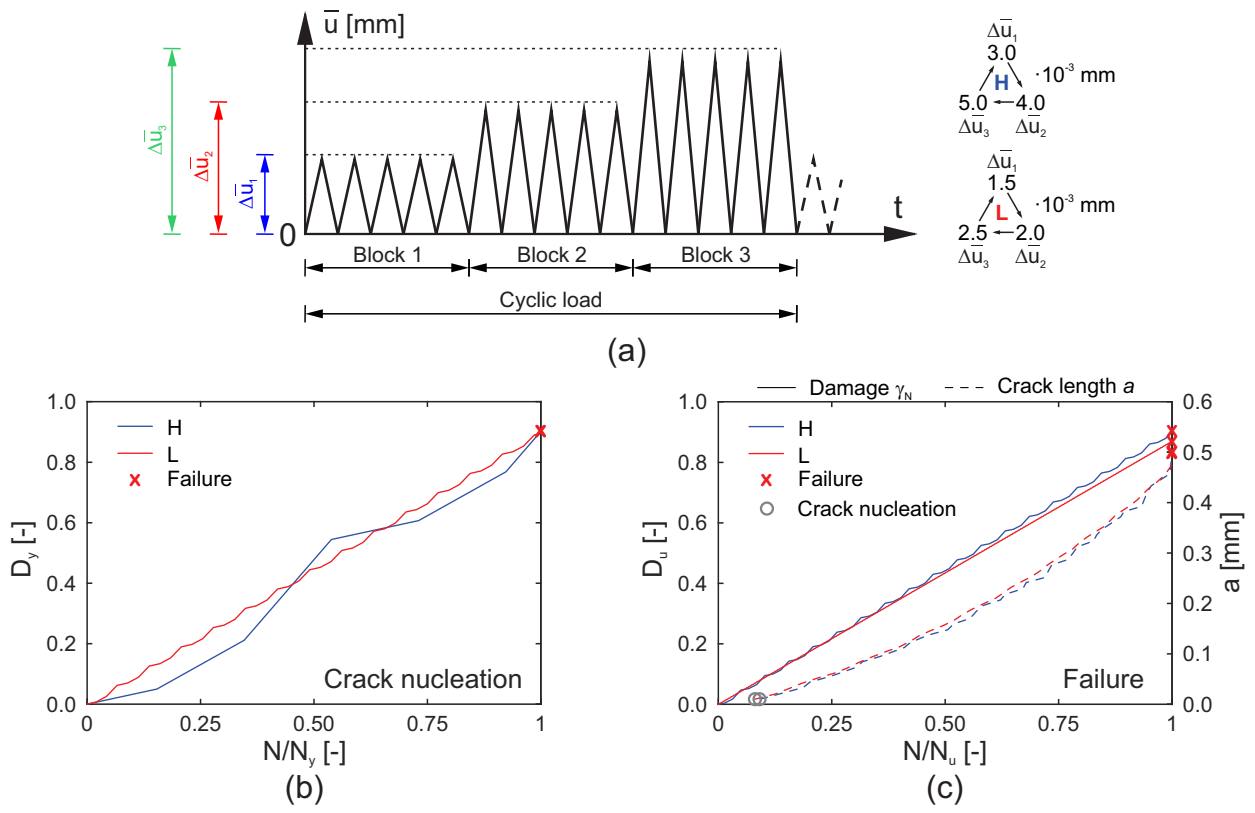


Fig. 7: (a) Sequential multiblock cyclic load and accumulation of the Palmgren-Miner-type damage γ_N for (b) crack nucleation and (c) failure (along with the final fatigue life curve).

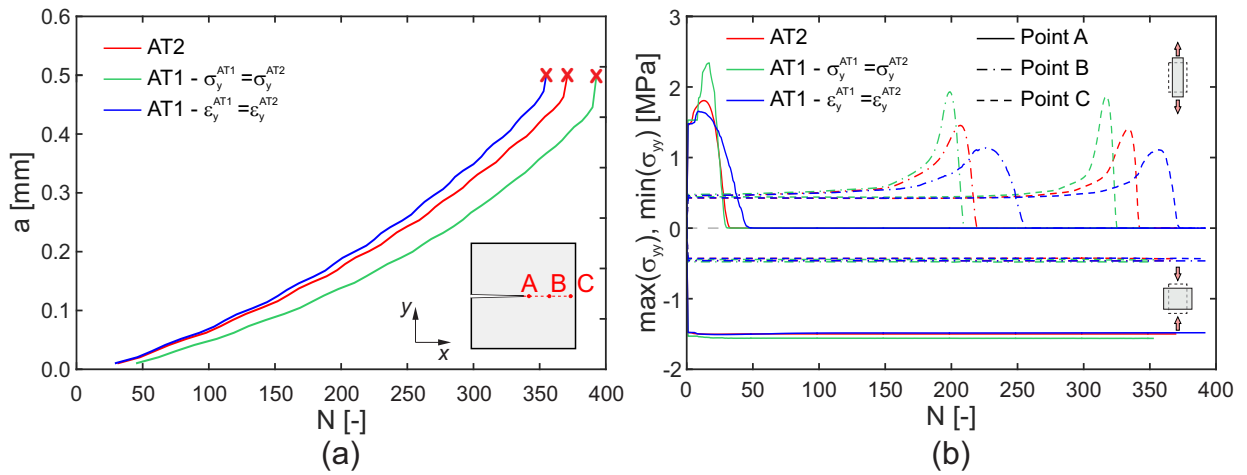


Fig. 8: (a) Fatigue life curves adopting the AT2 or AT1 model and (b) maximum and minimum value of σ_{yy} vs. cycle number N .

More differences can be observed by comparing the local behavior. Fig. 8b shows the maximum and minimum value of σ_{yy} reached in each cycle for the points A, B and C sketched in Fig. 8a and located at the same height of the notch and at 0.01, 0.20 and 0.40 mm distance from its tip. Close to the notch tip, the accumulation of the fatigue history variable has less influence on the strength of the material because the softening phase is reached during the early stages of the test (Fig. 8b). Conversely, away from the notch tip, $\bar{\alpha}$ can increase significantly before the softening phase, leading to lower maximum stresses attainable.

Fig. 9a shows the results obtained adopting the logarithmic fatigue degradation function Eq. 38 for the same values of the material parameter κ of Fig. 2b. As expected, increasing the slope of the fatigue degradation function leads to a shorter fatigue life. However, if the number of cycles is normalized by N_u , we obtain again a single fatigue life curve. The evolution of the asymptotic and logarithmic degradation functions for the point A of Fig. 8a are compared in Fig. 9b. Here we can observe an initial phase where the functions are constant and equal to 1, followed by a decreasing branch that ends with a plateau, starting when the phase field variable in A attains the unity and the fatigue history variable cannot evolve anymore.

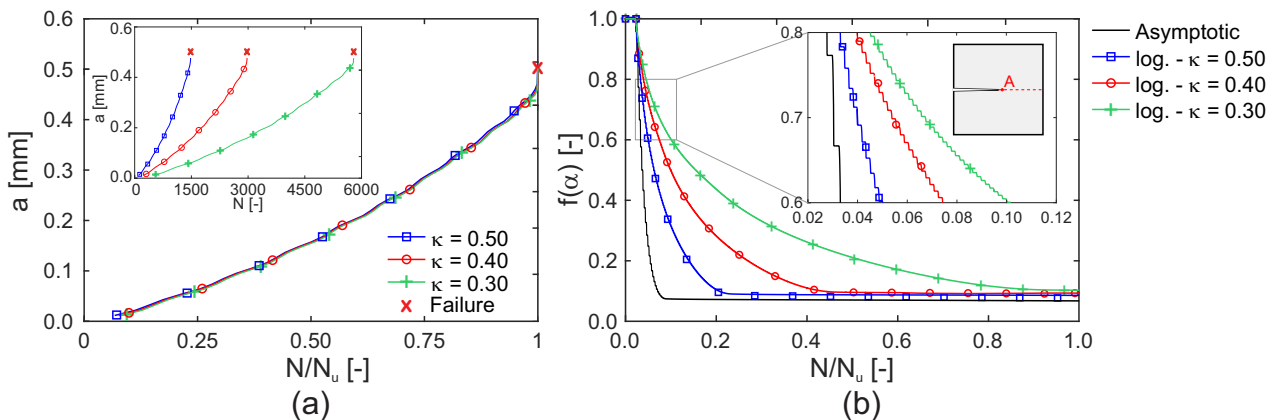


Fig. 9: Fatigue life prediction using the logarithmic fatigue degradation function $f(\alpha)$ (Eq. 38): (a) fatigue life curves for different κ parameters and (b) pertaining evolution of $f(\alpha)$ and comparison with the asymptotic fatigue degradation function (Eq. 37).

A further test is performed by subjecting the single-edge notched specimen to shear loading, see Fig. 3b. First, a non-inverting displacement is applied with range $\Delta\bar{u} = 3 \cdot 10^{-3}$ mm (Fig. 10a). The results in terms of cumulated history and phase-field variables are reported in Figs. 10b,c and d respectively for nucleation, stable and unstable propagation of the crack. Here we can observe that, although the fatigue history variable $\bar{\alpha}$ is accumu-

lated in the whole domain over large regions, the observed crack maintains its localized nature and its path is similar to the one observed in the monotonic case, namely it originates at the initial notch tip and propagates downwards toward the lower right corner (Figs. 10b-d). A second test is performed by applying to the same specimen a symmetrically inverting displacement with range $\Delta\bar{u} = 6 \cdot 10^{-3} \text{mm}$ as shown in Fig. 10e. In this case the accumulation of $\bar{\alpha}$ and the evolution of the phase field variable d are different from the previous example. Two cracks branch from the tip of the initial notch and propagate symmetrically toward the top and bottom corners at the right-hand side (Figs. 10f-h). In particular, the upper and lower cracks are the result respectively of the negative and positive part of the cyclic load (Fig. 10e). The accumulation of $\bar{\alpha}$ spreads over even larger regions (Figs. 10f-h) but, again, the crack remains localized. This example also demonstrates the ability of the approach to handle branching cracks.

5.2. Comparison with Paris theory

In this section we compare the results of the proposed approach with the main features of the Paris theory in terms of both crack growth rate curves and parameters of the Paris law C and m . In particular, the importance of the Paris law lies in the fact that C and m are meant to be material parameters². Such condition is not met by the majority of the available approaches to fatigue, such as the Wöhler curve for which the parameters of the Basquin relationship (Eq. 1) change with varying geometry and boundary conditions. To test whether our approach recovers the Paris theory and whether the corresponding parameters depend or not on the test setup, we analyze and compare the results obtained simulating two popular tests to characterize the fatigue behavior of a brittle material, i.e. the *compact tension* (*CT*) and the *three-point-bending* (*TPB*) tests.

The material parameters adopted are $E = 6 \text{GPa}$, $\nu = 0.22$, $G_c = 2.28 \text{N/mm}$ ($K_{\text{IC}} = 3.69 \text{MPa}\sqrt{\text{m}}$), $\alpha_T = \alpha_N = 9.5 \cdot 10^{-1} \text{N/mm}^2$ and $\ell = 0.2 \text{mm}$. Plane stress conditions are assumed and the simulations are force-controlled. The positive (tensile) cyclic load is characterized by a range ΔP and minimum, maximum and mean load levels P_{\min} , P_{\max} and P_{mean} , respectively (Fig. 11).

The tests are performed following the guidelines ASTM E 647 [12] for the CT specimen and ASTM E 1820 [13] for the TPB specimen. The crack growth rate curve da/dN vs. ΔK is obtained numerically, approximating

²In case of non-linear fatigue behaviors the Paris parameters are no longer constant but, rather, functions of certain quantities. E.g., for mean load sensitive materials they are related to the mean load, see sect. 5.2.1.

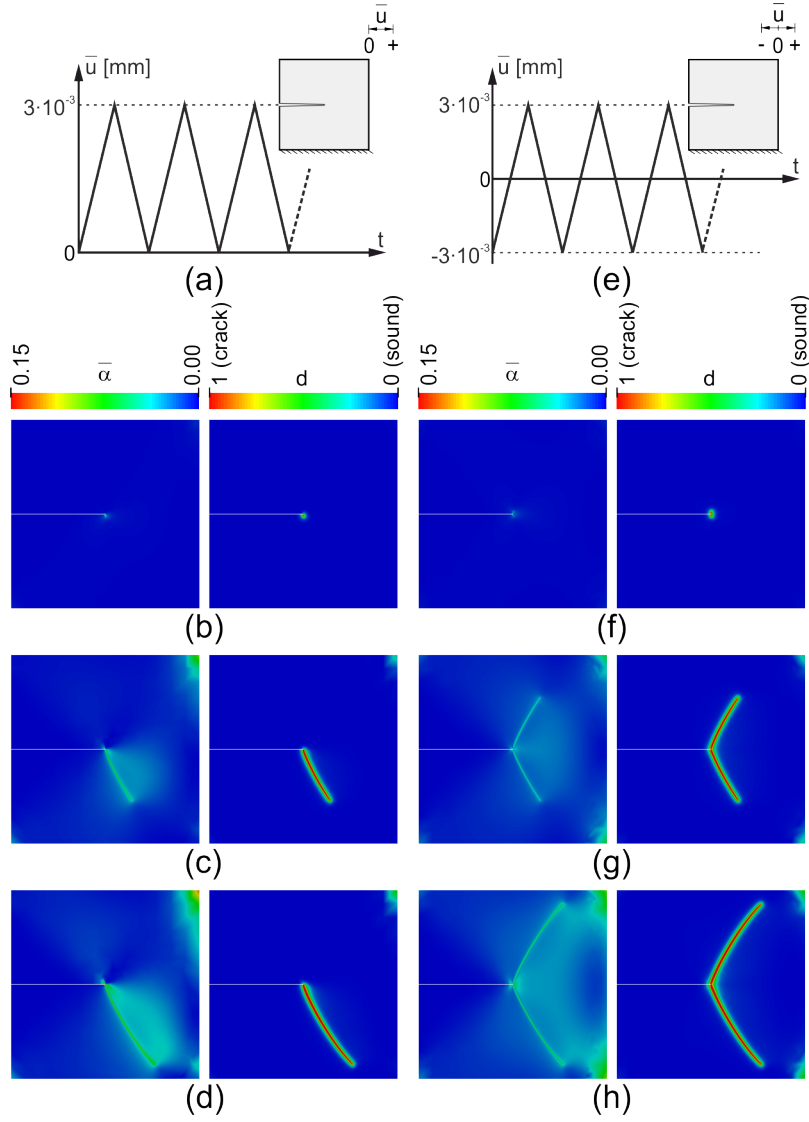


Fig. 10: Fatigue shear test for the single-edge notched specimen. (a) Non-inverting applied displacement and (b), (c), (d) fatigue history variable and phase-field maps respectively for crack nucleation, stable propagation and incipient failure. (e) Symmetrically inverting applied displacement and (f), (g), (h) fatigue history variable and phase-field maps respectively for crack nucleation, stable propagation and incipient failure.

the crack growth rate for sufficiently small crack length increment Δa as

$$\frac{da}{dN} \approx \frac{\Delta a}{\Delta N}, \quad (45)$$

where a constant value of $\Delta a \simeq 0.25$ mm is adopted as suggested in [12, 13].

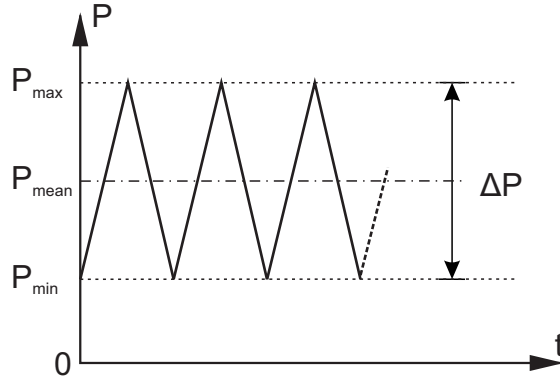


Fig. 11: Applied cyclic load.

The stress intensity factor range ΔK is obtained using the general expression

$$\Delta K = \frac{\Delta P}{T\sqrt{W}} Y\left(\frac{a}{W}\right), \quad (46)$$

where W and T are respectively a characteristic length and the thickness of the specimen and $Y(a/W)$ is a dimensionless geometric factor whose expression is given in [12, 13]. To obtain the Paris law parameters, the crack growth rate data lying in the Paris regime (i.e., for stable crack propagation) are best fitted to the Paris law to determine C and m in a double logarithmic plot. The algorithms adopted to obtain the numerical crack growth rate curves and the Paris parameters are detailed in Appendix B.

5.2.1. Compact tension (CT) specimen

The geometry and boundary conditions used for the CT tests are summarized in Fig. 12a along with the monotonic force-displacement curves for different lengths of the initial notch a_0 (Fig. 12b). As for Fig. 3b, also in this case some jumps in the load-displacement curve are observed in the post-peak regime. They are here followed by a limited hardening branch again due to short phases of unstable propagation of the crack, whose tip can reach regions where the fatigue history variable $\bar{\alpha}$ is lower than the threshold value α_T and the fracture toughness is thus still the same of the virgin material.

For a fixed geometry, the range of the stress intensity factor ΔK is related only to ΔP and a (Eq. 46). Hence, following the Paris theory, the crack growth rate obtained changing the load range ΔP or the initial notch a_0 should be the same provided ΔK is the same. Fig. 13 presents the results of different simulations of a cyclic test on the CT specimen varying either ΔP or a_0/W while keeping the other parameters the same according to Tab. 2.

Specimen	a_0/W [-]	ΔP [N]	P_{max}/P_{mon} [-]	N_u [-]	C	m
CT		10.0	6.7%*	60974	$2.15 \cdot 10^{-2}$	3.25
CT		15.0	10.1%*	17690	$2.12 \cdot 10^{-2}$	3.38
CT		20.0	13.5%*	7288	$2.01 \cdot 10^{-2}$	3.42
CT		40.0	26.9%*	817	$1.60 \cdot 10^{-2}$	3.73
CT		60.0	40.4% \diamond	210	-	-
CT	0.22	80.0	53.8% \diamond	71	-	-
CT		100.0	67.3% \diamond	27	-	-
CT		110.0	74.0% \diamond	16	-	-
CT		120.0	80.8% \diamond	9	-	-
CT		130.0	87.5% \diamond	4	-	-
CT		140.0	94.2% \diamond	1	-	-
CT	0.30		16.5%*	3645	$1.98 \cdot 10^{-2}$	3.50
CT	0.40	20.0	21.4%*	1483	$1.85 \cdot 10^{-2}$	3.61
CT	0.50		28.9%*	512	$1.57 \cdot 10^{-2}$	3.83
CT	0.60		41.2% \diamond	129	-	-
TPB		4.0	6.9%*	41823	$1.81 \cdot 10^{-2}$	3.25
TPB		5.0	8.7%*	21198	$1.80 \cdot 10^{-2}$	3.30
TPB		7.5	13.0%*	6100	$1.73 \cdot 10^{-2}$	3.33
TPB		10.0	17.3%*	2493	$1.67 \cdot 10^{-2}$	3.42
TPB		15.0	26.0%*	688	$1.52 \cdot 10^{-2}$	3.60
TPB	0.45	20.0	34.6%*	266	$1.29 \cdot 10^{-2}$	3.86
TPB		25.0	43.2% \diamond	123	-	-
TPB		30.0	51.9% \diamond	62	-	-
TPB		35.0	60.6% \diamond	33	-	-
TPB		40.0	69.2% \diamond	18	-	-
TPB		45.0	77.9% \diamond	9	-	-
TPB		50.0	86.5% \diamond	4	-	-
TPB		57.5	99.5% \diamond	1	-	-
Average					$1.78 \cdot 10^{-2}$	3.50

Tab. 2: Paris law parameters obtained for the CT and TPB specimens from the curves of Figs. 13 and 17.

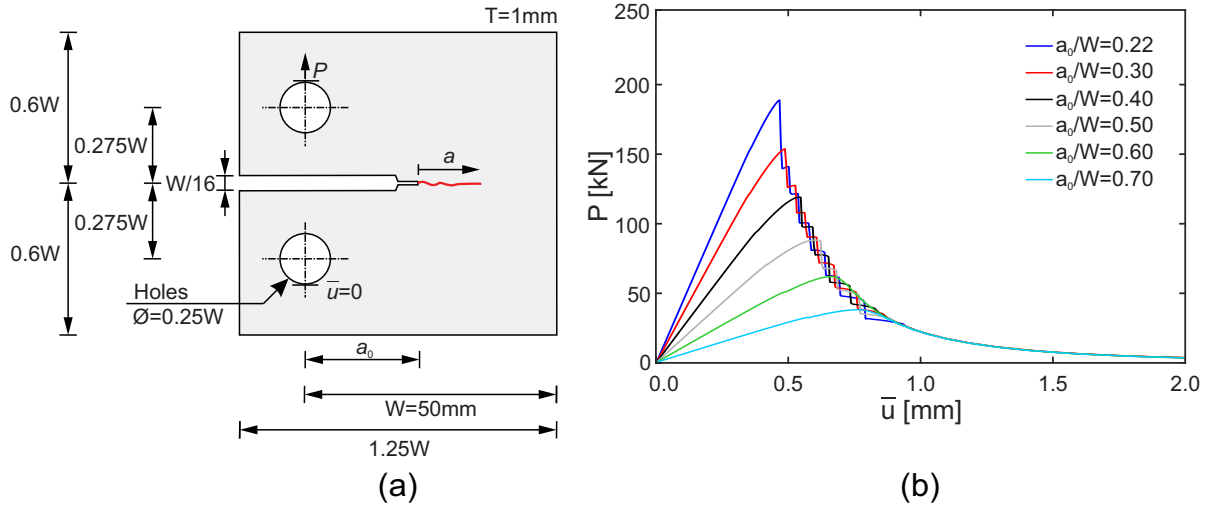


Fig. 12: CT specimen: (a) geometry and boundary conditions and (b) monotonic load-displacement curves for different lengths of the initial notch.

Unlike the standard Paris law, the proposed framework is able to recover all the three branches of the experimental crack growth rate curve, featuring an initial short non-linear nucleation phase followed by a linear stable crack propagation branch and, ultimately, by unstable crack propagation (Fig. 13). Also, most of the stable propagation branches of the curves cluster together, with the exception of a few cases (marked with a \diamond in Fig. 13) where the ratio between the maximum load in a cycle P_{max} and the maximum monotonic load P_{mon} is quite high (Tab. 2). For these tests the fatigue life N_u is very limited (i.e., less than 500 cycles), leading to oligocyclic fatigue where the fatigue degradation mechanism cannot develop completely since the damage process dominates. Here the nucleation and unstable crack propagation phases are so close to interfere with each other. A further evidence for a change in the failure mechanism from damage- to fatigue-dominated is given by the modified Wöhler curve relating the ratio P_{max}/P_{mon} to the maximum number of cycles before failure N_u , presented in Fig. 14. For the fatigue model adopted here and based on Fig. 14 the limit between the two regimes is close to $P_{max}/P_{mon} \simeq 40\%$.

For the curves with $P_{max}/P_{mon} > 40\%$ that feature a clear stable propagation regime (marked with \star in Fig. 13), it is possible to obtain the Paris law parameters through the procedure illustrated in Appendix B. The parameters obtained from the different curves are very close (Tab. 2) especially the slope m . This confirms that they are material properties which characterize the fatigue behavior, suggesting that the Paris theory is fully recovered by

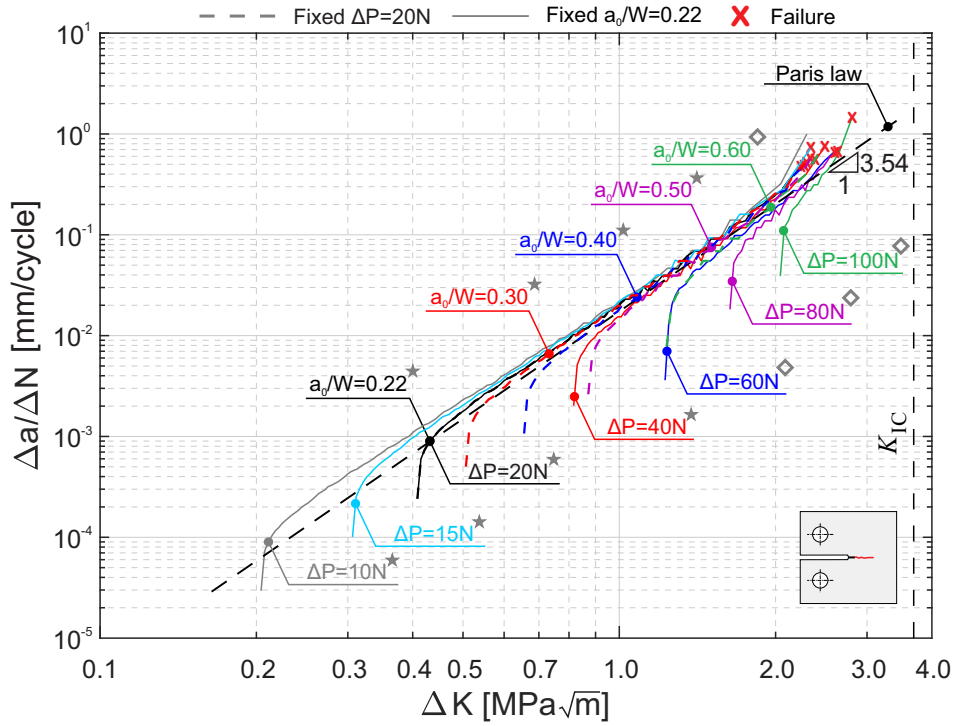


Fig. 13: Fatigue crack growth rate curves for the CT specimen varying the length of the initial notch and load range. (\star curves used to obtain the Paris law parameters in Tab. 2; \diamond curves not used to obtain the Paris law parameters because of the absence or scarce extension of the Paris regime.)

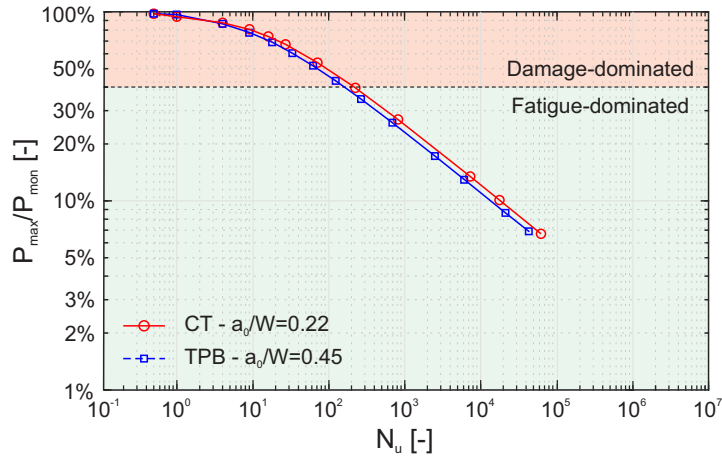


Fig. 14: Modified Wöhler curve for the CT and TPB specimens from Tab. 2.

the proposed framework. Note that this result is reached with no fine tuning of the parameters, nor by enforcing a priori the presence of a Paris regime,

nor imposing it to be common to all values of ΔP and a_0 .

Fig. 15 shows the effects of P_{mean} as given by Eq. 36 and of the adoption of the logarithmic fatigue degradation function Eq. 38 on the crack growth rate curves. The curve of Fig. 13 for the CT specimen with $a_0/W=0.22$ and $\Delta P=40\text{N}$ (mean load $P_{mean}=20\text{N}$) is used as a reference curve (dashed gray line in Fig. 15). Adopting Eq. 36 and varying only P_{mean} leads to curves whose trend is similar to the reference one but shifted in the $\Delta a/\Delta N$ - ΔK plane of a quantity dependent on the parameter α_N of Eq. 36 (Fig. 15a). Comparing the mean load sensitive curves, one can notice that they are shifted toward higher crack growth rates as the mean load increases. This observation is confirmed by the Paris parameters obtained in Tab. 3, which show negligible differences in m and largely different values of C .

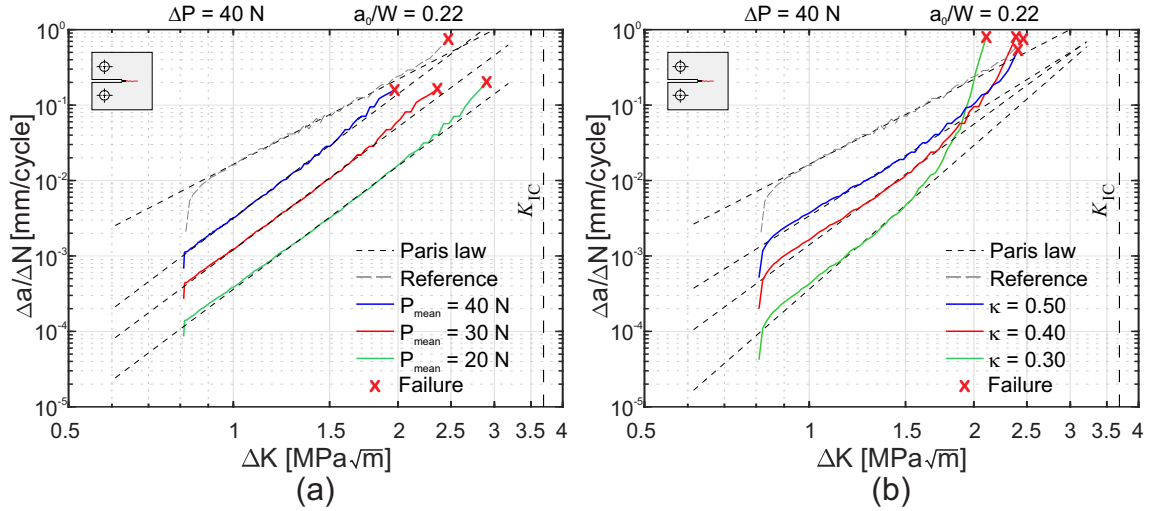


Fig. 15: Comparison between a reference fatigue crack growth rate curve obtained using the mean load insensitive accumulation function (Eq. 35) and the asymptotic fatigue degradation function (Eq. 37) and those obtained adopting (a) the mean load dependent accumulation function (Eq. 36) for different mean load values P_{mean} and (b) the logarithmic fatigue degradation function (Eq. 38) for different κ values.

Fig. 15b compares the reference curve with the results obtained adopting the logarithmic fatigue degradation function Eq. 38 for different values of κ . The parameter κ permits to control both C and m . As highlighted also by Tab. 3, an increasing κ leads to higher crack growth rates and lower slopes of the linear branch.

5.2.2. Three-point bending specimen

Aim of this section is to compare the results obtained for the CT specimen with those obtained with a TPB specimen, keeping the material parameters

Curve	ΔP [N]	a_0/W [-]	C	m
Reference	40	0.22	$1.60 \cdot 10^{-2}$	3.73
$P_{mean}=20$ N			$3.56 \cdot 10^{-4}$	5.42
$P_{mean}=30$ N	40	0.22	$1.19 \cdot 10^{-3}$	5.39
$P_{mean}=40$ N			$3.15 \cdot 10^{-3}$	5.48
$\kappa=0.30$			$3.38 \cdot 10^{-4}$	6.32
$\kappa=0.40$	40	0.22	$1.32 \cdot 10^{-3}$	5.30
$\kappa=0.50$			$3.21 \cdot 10^{-3}$	4.53

Tab. 3: Paris law parameters obtained from the curves of Fig. 15.

unchanged. The geometry of the TPB specimen is illustrated in Fig. 16a along with the monotonic load-displacement curve (Fig. 16b), which features a similar post-peak snap-back/local hardening behavior as previously shown for the CT specimen.

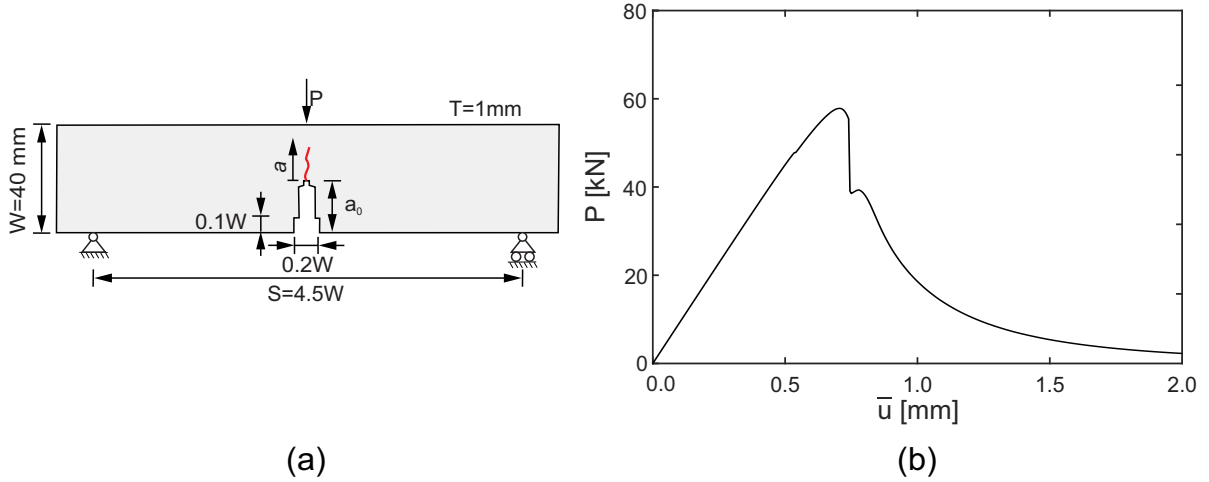


Fig. 16: TPB specimen: (a) geometry and boundary conditions and (b) monotonic load-displacement curves.

The results obtained in terms of crack growth rate curves for different load ranges ΔP are illustrated in Fig. 17, where those obtained for the CT specimen are also reported with gray dashed lines. The results are qualitatively and quantitatively very similar both among the TPB test series and between the latter and those of the CT specimen. The TPB specimen shows as well a transition between damage- and fatigue-dominated behavior (Fig. 14) with a

curve almost identical to the one related to the CT specimens. In particular, the transition takes place for similar P_{max}/P_{mon} ratios, i.e., close to 40%.

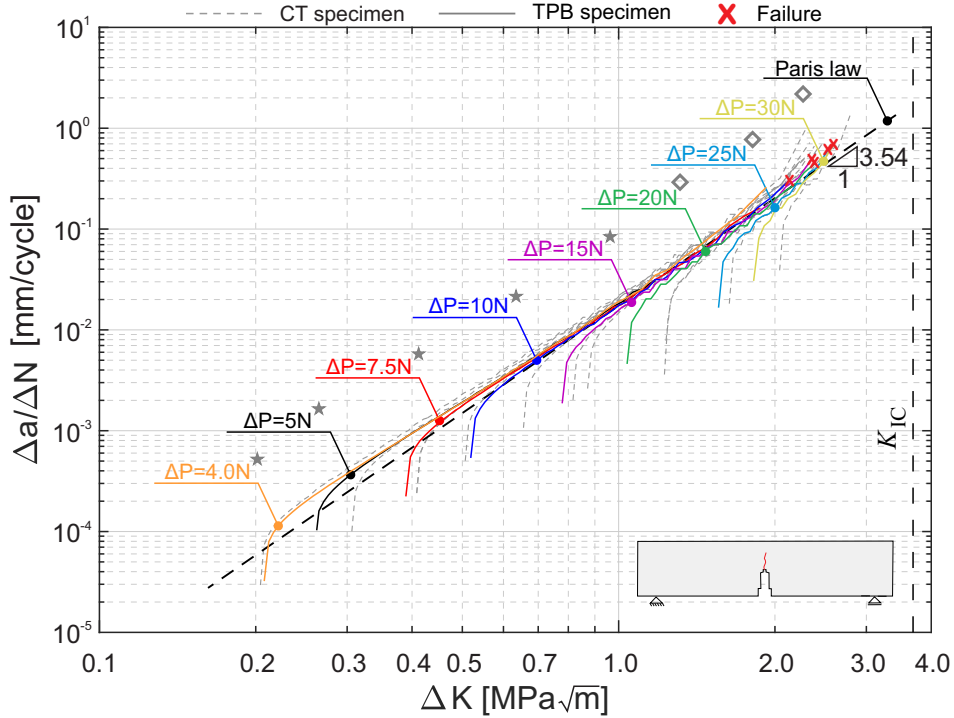


Fig. 17: Fatigue crack growth rate curves for the TPB specimen with varying load range and comparison with the CT specimen results. (\star curves used to obtain the Paris law parameters in Tab. 2; \diamond curves not used to obtain the Paris law parameters because of the absence or scarce extension of the Paris regime.)

The Paris parameters for the TPB case are reported in Tab. 2. Again, the values are very similar to each other and to those of the CT test.

Summing up, the proposed framework reproduces the main features of the Paris theory, including also the nucleation and unstable propagation phases. Moreover, it reproduces a Wöhler-like curve capturing the transition between damage- and fatigue-dominated processes.

5.3. Complex geometries and loading conditions

After showing that the proposed framework includes and extends the Paris law for brittle materials, we subsequently demonstrate that adopting the phase-field description of fracture it is possible to deal with complex geometries and loading conditions in 2- and 3-D, which lead to nucleation and propagation of multiple cracks with arbitrarily complex topologies.

5.3.1. Plate with holes

In this example we study the behavior of a homogeneous plate with 23 uniformly or randomly distributed holes subjected to different loading cycles, including pure compressive and tensile-compressive fatigue. Similar tests, but under monotonic compressive loadings, are investigated experimentally in [52] and numerically in [53]. The material parameters are $E = 12$ GPa, $\nu = 0.22$, $G_c = 1.40 \cdot 10^{-3}$ N/mm, $\alpha_T = 6.480 \cdot 10^{-3}$ N/mm² and $\ell = 0.018$ mm as in [53]. Plane strain conditions, displacement control and a uniform spatial discretization with $h = \frac{\ell}{3}$ in the whole domain are assumed.

Before showing results of the fatigue tests on the actual specimens, a premise regarding the choice of the split in compressive tests is needed. When brittle materials are subjected to pure compression, the resulting failure mechanism is characterized by cracks oriented in the direction orthogonal to the principal tensile stress. These cracks nucleate at voids or other (micro-) heterogeneities of the material. This is usually termed axial splitting failure mode [49]. To capture this behavior the no-tension split is developed in [54]. To show this we simulate a monotonic compression test of a plate with a single hole, whose geometry and boundary conditions are given in Fig. 18a. Comparing the resulting crack patterns for the volumetric/deviatoric, spectral and no-tension split (Figs. 18b, c and d respectively) it is clear that only the latter reproduces the splitting failure. For this reason, in the fatigue tests under compressive loading described as follows the no-tension split is adopted.

The first test involves a plate with uniformly distributed holes subjected to a cyclic compressive load as depicted in Fig. 19a. The phase-field contours at the nucleation (on the left), stable propagation (in the center) and incipient failure phase (on the right) are presented in Fig. 19b, where we can observe that the model is naturally able to handle the presence of different cracks. Moreover, the final crack patterns obtained in the cyclic and monotonic case (the latter is not shown here but very similar to the right contour of Fig. 19b) is in good agreement with what observed experimentally in [52] and numerically in [53]. The other two tests are related to an alternate tension-compression cyclic load applied to plates with uniformly (Fig. 19c) and randomly (Fig. 19e) distributed holes. The crack patterns at crack nucleation (on the left), stable propagation (in the center) and right before failure (on the right) are depicted in Figs 19d,e, showing that with the proposed approach it is possible to reproduce complex fracture patterns with many cracks interacting with each other, branching and merging until failure of the specimen. Note that the study of these examples with standard techniques based on the Paris law is rather complicated since it needs the

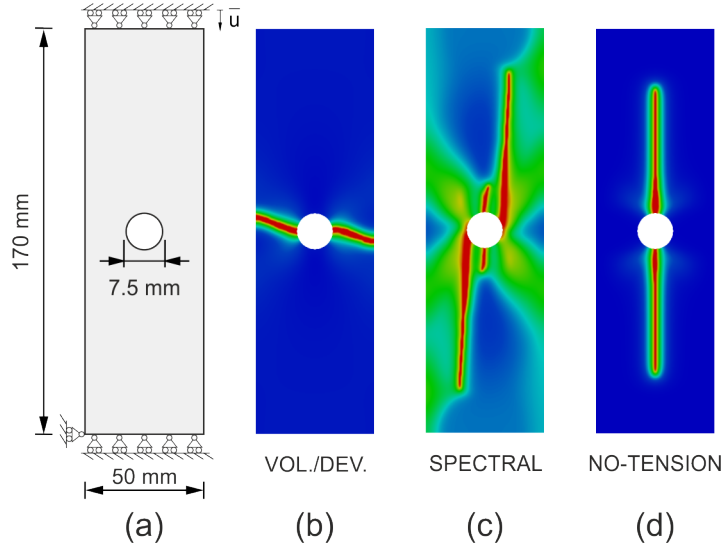


Fig. 18: Compression test of a plate with a single hole. (a) Geometry and boundary conditions and results adopting (b) the volumetric/deviatoric split, (c) the spectral split and (d) the no-tension split showing the correct axial splitting failure mechanism.

definition of the stress intensity factor range for each crack, which strongly depends on the evolution of the neighboring ones.

5.3.2. 3-D geometry: steering arm

This example aims at investigating the fatigue behavior of a real 3-D component subjected to fatigue. In particular, the steering arm investigated in [16] with the geometry illustrated in Fig. 20a is considered. The material parameters adopted are $E = 110$ GPa, $\nu = 0.30$, $G_c = 0.40$ N/mm, $\alpha_T = 4.761 \cdot 10^{-2}$ N/mm² and $\ell = 0.7$ mm. Figs. 20b-d illustrate the predicted crack pattern for a monotonic load in positive x direction applied to the internal surface of the upper ring with different boundary conditions. For all the tests the bottom surface of the base and the inner surfaces of the two base holes are fixed in all directions. In case 1 (Fig. 20b) there is a notch in the lower part of the shaft as in [16], in case 2 there is no notch (Fig. 20c) and case 3 (Fig. 20d) is the same as case 2 but the inner surface of the upper ring is fixed in the y and z directions. We can see that, if no notch is a priori assumed, the crack can nucleate at both top (case 3) or bottom (case 2) of the shaft depending on the boundary conditions.

Applying a cyclic displacement with range $\Delta \bar{u} = 3.5 \cdot 10^{-2}$ mm in positive x direction the crack nucleates at the location of the monotonic case for all of the three cases analyzed (Fig. 21a-c). For the case 2 a limited evolution of the phase-field variable, i.e. $d \leq 0.7$, below the upper ring is visible

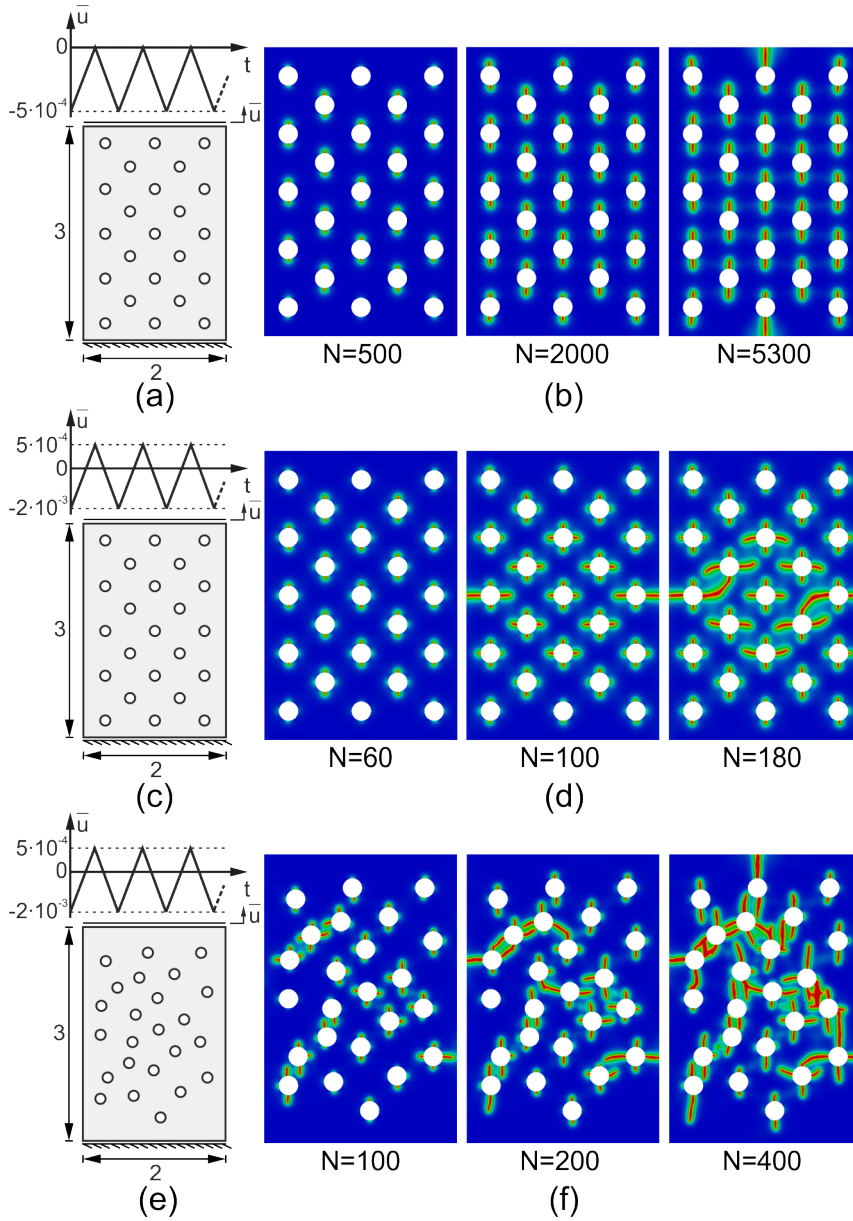


Fig. 19: Cyclic test on a plate with 23 holes. Geometry and boundary conditions for (a) plate with uniformly distributed holes and purely compressive load, (c) plate with uniformly distributed holes and tensile-compressive load and (e) plate with randomly distributed holes and tensile-compressive load. (b), (d) and (f) show the phase-field contours at crack nucleation (on the left), stable propagation (in the center) and incipient failure (on the right) respectively for the setups (a), (c) and (e).

(Fig. 21b), which however stops after the nucleation of the main crack in the lower section of the shaft. The final crack pattern for case 1 and case 2 is very

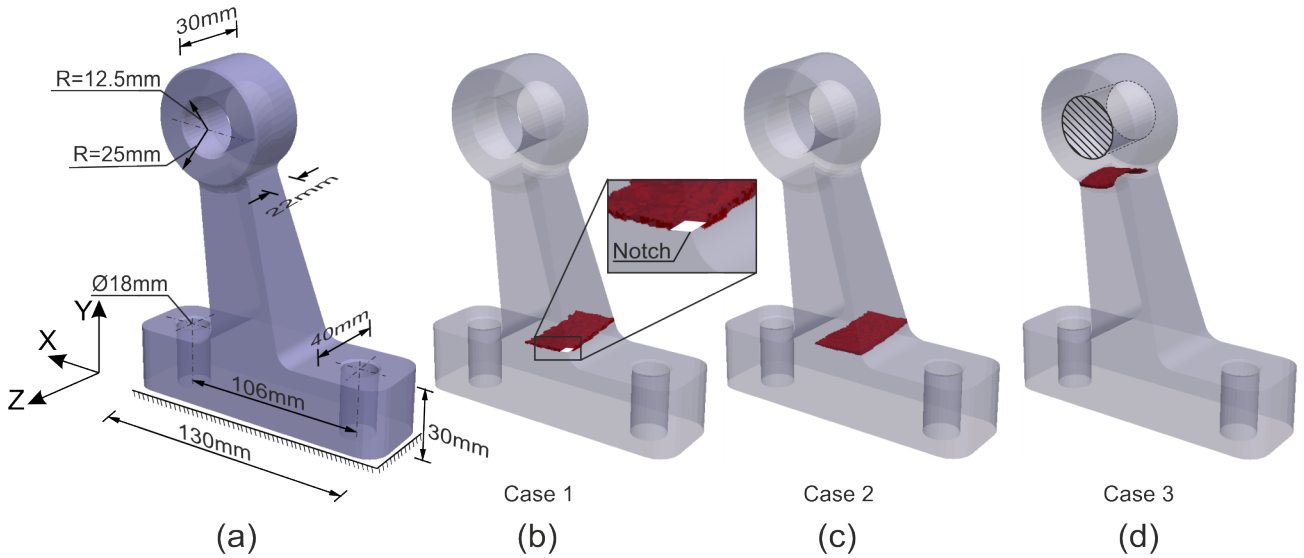


Fig. 20: Steering arm: (a) geometry and crack pattern at failure under monotonic loading for (b) case1, (c) case 2 and (d) case 3.

similar to the monotonic case (Figs. 20b-c), while for case3 two cracks are present, the one responsible for failure below the upper ring and a secondary one in the lower part of the shaft (Fig. 20d).

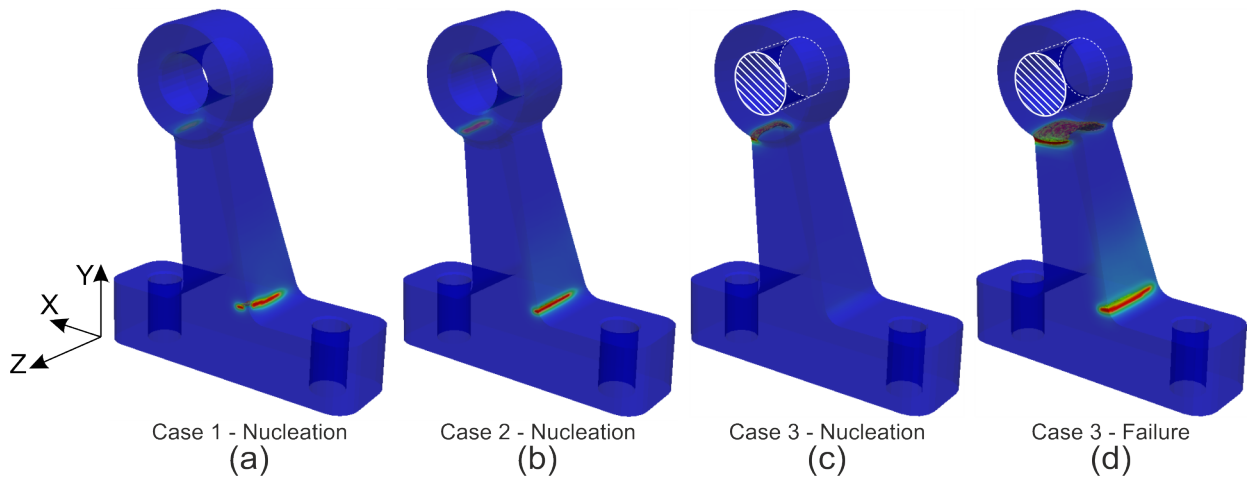


Fig. 21: Fatigue test with displacement applied in positive x direction: crack nucleation for (a) case1, (b) case 2, (c) case 3 and (d) final crack pattern for case 3.

A further test, case 4, is performed by applying to case 3 a symmetric displacement in positive and negative x directions with range $\Delta \bar{u} = 5 \cdot 10^{-2} \text{mm}$. In this case, the crack pattern becomes more complicated, with two compet-

ing cracks nucleating at the top of the shaft that finally cause the failure of the component (Fig. 22). In particular, a crack nucleates first as in **case 3** (Fig. 22a), while a second one appears later on the opposite side as a result of the negative displacement (Fig. 22b).

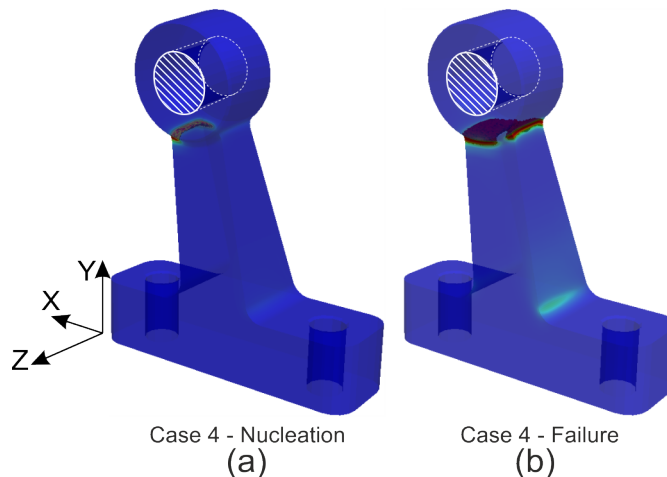


Fig. 22: Fatigue test with displacement applied symmetrically in positive and negative x directions (case 4): (a) crack nucleation and (b) final crack pattern.

The study of the component of Fig. 20a using standard methods as in [16] is possible only assuming an initial notch, which is usually the result of the early stage of the service life. However, imposing a priori shape and position for such a notch in a complex case such as the one studied here is not trivial, being a function of loading and boundary conditions. Conversely, the proposed framework is naturally able to let the fracture nucleate at the most stressed regions.

6. Conclusions

A novel framework to model fatigue in brittle materials based on the variational phase-field approach to fracture is proposed. The standard phase-field free energy functional is modified so as to allow the fracture toughness of the material to decrease as a suitable fatigue scalar history variable increases. The reduction rate is governed by a fatigue degradation function that acts as a fatigue constitutive equation and takes as argument only the fatigue history variable. The choice of both history variable and fatigue degradation function is very flexible, being subjected only to some general requirements. In the present work, the fatigue history variable is assumed as the cumulated active part of the elastic strain energy density. Two definitions of the cumulated variable and two fatigue degradation functions are proposed, allowing

to reproduce the major fatigue characteristics of different brittle materials. Depending on the specific choice, a maximum of three additional parameters is required.

Based on the obtained results the following conclusions can be drawn:

- the proposed framework reproduces the Paris theory for fatigue crack growth in brittle materials, encompassing naturally also the nucleation and unstable propagation phases besides the Paris regime;
- in addition it enables the computation of the parameters of the Paris law and extensions thereof;
- the Wöhler or $S - N$ curve and the transition between damage- and fatigue-dominated regimes are also naturally reproduced;
- the Palmgren-Miner rule and the behavior under monotonic loading are obtained as special cases;
- the proposed approach is able to naturally handle complex geometries, loading conditions and fracture patterns including multiple cracks with arbitrary topology also in 3-D.

Appendix A. Relation between the Miner rule and the Paris law

Eq. 46 can be recasted in the form

$$\Delta K = y(a)\Delta P\sqrt{\pi a}, \quad (\text{A.1})$$

where $y(a)$ is a modified geometric factor. Substituting Eq. A.1 into Eq. 3 we have

$$\frac{da}{dN} = C\pi^{m/2}y(a)^m\Delta P^m a^{m/2}. \quad (\text{A.2})$$

Integrating Eq. A.2 over a single cycle N_i , assuming a_i (a_{i+1}) is the initial (final) crack length and that $y(a) = y(a_i)$ is cycle-wise constant we obtain

$$a_{i+1}^{1-m/2} - a_i^{1-m/2} = \left(1 - \frac{m}{2}\right) C\pi^{m/2}y(a_i)^m\Delta P^m = \beta (y(a_i)\Delta P)^m, \quad (\text{A.3})$$

where $\beta = \left(1 - \frac{m}{2}\right) C\pi^{m/2}$ is a constant.

From Eq. A.3 it is clear that the crack advancement in a single cycle depends on the current length of the crack. Hence, the contribution of the i -th cycle to the crack growth is history dependent. In order to comply with

the Palmgren-Miner assumption the right-hand-side of Eq. A.3 needs to be independent on the current crack length a_i , so that the order of the cycles does not influence the crack growth. Such condition can be met cycle-wise only if the geometric factor is constant, i.e. $y(a) = \bar{y}$ such as in the case of infinite domains [22], or changing ΔP to compensate the variation of $y(a)$ so that $(y(a_i)\Delta P)^m$ is constant. Since $y(a)$ is generally a monotonic increasing function of a , the applied load should decrease with the crack advancement.

Appendix B. Numerical evaluation of the crack growth rate curve

The numerical evaluation of the crack growth rate curve and of the Paris law is performed following the standard guidelines ASTM E 647 [12] and ASTM E 1820 [13]. Defining as a_n and a_{n+1} the crack length at the cycle N_n and N_{n+1} respectively, the crack growth rate, which is assumed to remain constant for sufficiently small crack length increments $\Delta a = a_{n+1} - a_n$, is obtained as

$$\left(\frac{\Delta a}{\Delta N}\right)_{n+1/2} = \frac{\Delta a}{N_{n+1} - N_n}, \quad (\text{B.1})$$

where $\Delta a \simeq 0.25$ mm [12, 13]. The corresponding stress intensity factor range reads

$$\Delta K_{n+1/2} = \frac{\Delta P}{T\sqrt{W}} Y_{n+1/2} \left(\gamma_{n+1/2} = \frac{a_{n+1/2}}{W}\right), \quad (\text{B.2})$$

where $a_{n+1/2} = \frac{1}{2}(a_{n+1} + a_n)$ is the average crack length and the geometric factor for the CT specimen is

$$Y_{n+1/2}(\gamma_{n+1/2}) = \frac{(2 + \gamma_{n+1/2})}{(1 - \gamma_{n+1/2})^{3/2}} (0.886 + 4.64\gamma_{n+1/2} + \\ -13.32\gamma_{n+1/2}^2 + 14.72\gamma_{n+1/2}^3 - 5.6\gamma_{n+1/2}^4), \quad (\text{B.3})$$

while for TPB specimen it is

$$Y_{n+1/2}(\gamma_{n+1/2}) = \frac{(3\frac{S}{W}\gamma_{n+1/2})}{2(1 + 2\gamma_{n+1/2})(1 - \gamma_{n+1/2})^{3/2}} (1.99 - \gamma_{n+1/2}(1 - \gamma_{n+1/2}) \\ (2.15 - 3.93\gamma_{n+1/2} + 2.7\gamma_{n+1/2}^2)). \quad (\text{B.4})$$

Once the crack growth rate curve is available, the parameters of the Paris law can be obtained by a linear regression in the double logarithmic plot

of the linear stable propagation phase. In this work, the linear regression is performed on the points included in the central third portion of the ΔK range spanned during the test. The resulting parameters are reported in Tab. 2.

Acknowledgments

This work was funded by the DFG through the Research Training Group 2075 "Modelling the constitutive evolution of building materials and structures with respect to aging" and the Priority Program 2020 "Cyclic deterioration of High-Performance Concrete in an experimental-virtual lab" along with the MIUR-DAAD Joint Mobility Program project "Variational approach to fatigue phenomena with phase-field models: modeling, numerics and experiments". Prof. Meinhard Kuna is gratefully acknowledged for providing the 3-D geometry of the steering arm of sect. 5.3.2.

References

References

- [1] P. Carrara, L. De Lorenzis, A coupled damage-plasticity model for the cyclic behavior of shear-loaded interfaces, *Journal of the Mechanics and Physics of Solids* 85 (2015) 33–53.
- [2] J. Newman, The merging of fatigue and fracture mechanics concepts: a historical perspective, *Progress in Aerospace Sciences* 34 (5-6) (1998) 347–390.
- [3] J. Schijve, Fatigue of structures and materials in the 20th century and the state of the art, *International Journal of Fatigue* 25 (8) (2003) 679–702.
- [4] S. Suresh, *Fatigue of Materials*, Cambridge University Press, Cambridge, 1998.
- [5] A. Wöhler, Über die festigkeits-versuche mit eisen und stahl, *Zeitschrift für Bauwesen* (XX) (1870) 73–106.
- [6] A. Palmgren, The service life of ball bearings, *Zeitschrift des Vereines Deutscher Ingenieure* (1924) 339–341.
- [7] M. A. Miner, Cumulative damage in fatigue, *Journal of Applied Mechanics* 12 (September) (1945) A159–A164.

- [8] A. Griffith, The phenomena of rupture and flow in solids, *Philosophical transactions of the royal society of London A: Mathematics, Physics and Engineering Sciences* 221 (1921) 163–198.
- [9] P. Paris, M. P. Gomez, W. E. Anderson, A rational analytic theory of fatigue 13 (4) (1961) 9–14.
- [10] G. Irwin, Analysis of Stresses and Strains near the End of a Crack Traversing a Plate,, *Journal of Applied Mechanics-Transactions of the ASME* E24 (1957) 351–369.
- [11] P. Paris, F. Erdogan, A critical analysis of crack propagation laws, *Journal of Basic Engineering* 85 (4) (1963) 528–533.
- [12] ASTM International, E647-05 Standard Test Method for Measurement of Fatigue Crack Growth Rates, ASTM International, West Conshohocken, PA, USA, 2005.
- [13] ASTM International, E1820-01 Standard Test Method for Measurement of Fatigue Crack Growth Rates, ASTM International, West Conshohocken, PA, USA, 2008.
- [14] S. R. Mettu, V. Shivakumar, J. M. Beek, F. Yeh, L. C. Williams, R. G. Forman, J. J. McMahon, J. Newman, J. C., NASGRO 3.0 : A software for analyzing aging aircraft, NASA Technical report (1999) 792–801.
- [15] W. Elber, Fatigue crack closure under cyclic tension, *Engineering Fracture Mechanics* 2 (1) (1970) 37–45, [arXiv:arXiv:1011.1669v3](https://arxiv.org/abs/1011.1669v3).
- [16] F. Rabold, M. Kuna, Automated Finite Element Simulation of Fatigue Crack Growth in Three-dimensional Structures with the Software System ProCrack, *Procedia Materials Science* 3 (2014) 1099–1104.
- [17] F. Rabold, M. Kuna, T. Leibel, Procrack: A software for simulating three-dimensional fatigue crack growth, *Lecture Notes in Applied and Computational Mechanics* 66 (2013) 355–374.
- [18] M. Ambati, T. Gerasimov, L. De Lorenzis, A review on phase-field models of brittle fracture and a new fast hybrid formulation, *Computational Mechanics* 55 (2) (2014) 383–405.
- [19] K. Rege, H. G. Lemu, A review of fatigue crack propagation modelling techniques using FEM and XFEM, *IOP Conference Series: Materials Science and Engineering* 276 (1).

- [20] R. Branco, F. V. Antunes, J. D. Costa, A review on 3D-FE adaptive remeshing techniques for crack growth modelling, *Engineering Fracture Mechanics* 141 (2015) 170–195.
- [21] R. Desmorat, Damage and fatigue - Continuum damage mechanics modeling for fatigue of materials and structures, *Revue Européenne de Génie Civil* 10 (6-7) (2006) 849–877.
- [22] H. Tada, P. C. Paris, G. R. Irwin, *The Stress Analysis of Cracks Handbook*, Third Edition, American Society of Mechanical Engineers, 2000.
- [23] Z. Sha, W. H. Wong, Q. Pei, P. S. Branicio, Z. Liu, T. Wang, T. Guo, H. Gao, Atomistic origin of size effects in fatigue behavior of metallic glasses, *Journal of the Mechanics and Physics of Solids* 104 (2017) 84–95.
- [24] S. Kozinov, M. Kuna, Simulation of fatigue damage in ferroelectric polycrystals under mechanical/electrical loading, *Journal of the Mechanics and Physics of Solids* 116 (2018) 150–170.
- [25] D. F. Li, R. A. Barrett, P. E. O’Donoghue, N. P. O’Dowd, S. B. Leen, A multi-scale crystal plasticity model for cyclic plasticity and low-cycle fatigue in a precipitate-strengthened steel at elevated temperature, *Journal of the Mechanics and Physics of Solids* 101 (2017) 44–62.
- [26] G. Zi, J. H. Song, E. Budyn, S. H. Lee, T. Belytschko, A method for growing multiple cracks without remeshing and its application to fatigue crack growth, *Modelling and Simulation in Materials Science and Engineering* 12 (5) (2004) 901–915.
- [27] E. Salvati, H. Zhang, K. S. Fong, X. Song, A. M. Korsunsky, Separating plasticity-induced closure and residual stress contributions to fatigue crack retardation following an overload, *Journal of the Mechanics and Physics of Solids* 98 (2017) 222–235.
- [28] Z. S. Hosseini, M. Dadfarnia, B. P. Somerday, P. Sofronis, R. O. Ritchie, On the theoretical modeling of fatigue crack growth, *Journal of the Mechanics and Physics of Solids* 121 (2018) 341–362.
- [29] S. Holopainen, R. Kouhia, T. Saksala, Continuum approach for modelling transversely isotropic high-cycle fatigue, *European Journal of Mechanics - A/Solids* 60 (2016) 183–195.
- [30] G. A. Francfort, J. J. Marigo, Revisiting brittle fracture as an energy minimization problem, *Journal of the Mechanics and Physics of Solids* 46 (8) (1998) 1319–1342.

- [31] B. Bourdin, G. A. Francfort, J. J. Marigo, Numerical experiments in revisited brittle fracture, *Journal of the Mechanics and Physics of Solids* 48 (4) (2000) 797–826.
- [32] K. Pham, H. Amor, J. J. Marigo, C. Maurini, Gradient damage models and their use to approximate brittle fracture, *International Journal of Damage Mechanics* 20 (4) (2011) 618–652.
- [33] J. L. Boldrini, E. A. Barros de Moraes, L. R. Chiarelli, F. G. Fumes, M. L. Bittencourt, A non-isothermal thermodynamically consistent phase field framework for structural damage and fatigue, *Computer Methods in Applied Mechanics and Engineering* 312 (2016) 395–427.
- [34] M. Caputo, M. Fabrizio, Damage and fatigue described by a fractional derivative model, *Journal of Computational Physics* 293 (2015) 400–408.
- [35] G. Amendola, M. Fabrizio, J. M. Golden, Thermomechanics of damage and fatigue by a phase field model, *Journal of Thermal Stresses* 39 (5) (2016) 487–499. [arXiv:1410.7042](#).
- [36] R. Alessi, S. Vidoli, L. De Lorenzis, A phenomenological approach to fatigue with a variational phase-field model: The one-dimensional case, *Engineering Fracture Mechanics* 190 (2018) 53–73.
- [37] R. Alessi, V. Crismale, G. Orlando, Fatigue effects in elastic materials with variational damage models: A vanishing viscosity approach (2018) 1–30, [arXiv:1807.04675](#).
- [38] C. Miehe, F. Welschinger, M. Hofacker, Thermodynamically consistent phase-field models of fracture: Variational principles and multi-field FE implementations (2010) 1273–1311.
- [39] A. Mielke, T. Roubíček, *Rate-Independent Systems*, Vol. 193 of Applied Mathematical Sciences, Springer New York, New York, NY, 2015.
- [40] A. Braides, A. Garroni, A remark on the nonlocal approximation of free-discontinuity problems, *Comm. Partial Differential Equations* 23 (1998) 817–829.
- [41] L. Ambrosio, V. Tortorelli, On the approximation of free discontinuity problems, *Bollettino dell’unione matematica italiana. B* 6 (1) (1992) 105–123.

- [42] R. Alessi, J. J. Marigo, S. Vidoli, Gradient damage models coupled with plasticity: Variational formulation and main properties, *Mechanics of Materials* 80 (2015) 351–367.
- [43] Z. A. Wilson, M. J. Borden, C. M. Landis, A phase-field model for fracture in piezoelectric ceramics, *International Journal of Fracture* 183 (2) (2013) 135–153.
- [44] C. Steinke, M. Kaliske, A phase-field crack model based on directional stress decomposition, *Computational Mechanics*.
- [45] E. Tanné, T. Li, B. Bourdin, J. J. Marigo, C. Maurini, Crack nucleation in variational phase-field models of brittle fracture, *Journal of the Mechanics and Physics of Solids* 110 (2018) 80–99.
- [46] G. Lancioni, G. Royer-Carfagni, The variational approach to fracture mechanics. a practical application to the french panthéon in Paris, *Journal of Elasticity* 95 (1-2) (2009) 1–30.
- [47] M. Strobl, T. Seelig, On constitutive assumptions in phase field approaches to brittle fracture, *Procedia Structural Integrity* 2 (2016) 3705–3712.
- [48] H. Amor, J. J. Marigo, C. Maurini, Regularized formulation of the variational brittle fracture with unilateral contact: Numerical experiments, *Journal of the Mechanics and Physics of Solids* 57 (8) (2009) 1209–1229.
- [49] F. Freddi, G. Royer-Carfagni, Regularized variational theories of fracture: A unified approach, *Journal of the Mechanics and Physics of Solids* 58 (8) (2010) 1154–1174.
- [50] A. Jaubert, J. J. Marigo, Justification of paris-type fatigue laws from cohesive forces model via a variational approach, *Continuum Mechanics and Thermodynamics* 18 (1-2) (2006) 23–45.
- [51] T. Gerasimov, L. De Lorenzis, On the penalization in variational phase-field models of brittle fracture, in preparation.
- [52] R. Romani, Rupture en compression des structures hétérogènes base de matériaux quasi-fragiles. PhD thesis. Paris VI: Université Pierre et Marie Curie, in preparation.
- [53] T. T. Nguyen, J. Yvonnet, M. Bornert, C. Chateau, K. Sab, R. Romani, R. Le Roy, On the choice of parameters in the phase field method for

simulating crack initiation with experimental validation, *International Journal of Fracture* 197 (2) (2016) 213–226.

- [54] F. Freddi, G. Royer-Carfagni, Variational fracture mechanics to model compressive splitting of masonry-like materials, *Annals of Solid and Structural Mechanics* 2 (2-4) (2011) 57–67.